SEMMELWEIS EGYETEM

DOKTORI ISKOLA

Ph.D. értekezések

3004.

VÁRNAI BIANKA

A gyógyszerészeti tudományok korszerű kutatási irányai
című program

Programvezető: Dr. Antal István, egyetemi tanár

Témavezető: Dr. Béni Szabolcs, egyetemi docens

Influencing Intermolecular Interactions: Exploring the Impact of Charge State on Cyclodextrins and Diverse Bioactive Guests

PhD thesis

Bianka Várnai

Semmelweis University Doctoral School

Pharmaceutical Sciences and Health Technologies Division

Supervisor: Szabolcs Béni, Ph.D.

Official reviewers: Arash Mirzahosseini, Ph.D.
Zoltán Fülöp, Ph.D.

Head of the Complex Examination Committee:
István Antal, Ph.D.

Members of the Complex Examination Committee:
Márta Mazákné Kraszni, Ph.D.
Éva Fenyvesi, Ph.D.

Budapest
2024

TABLE OF CONTENTS

LIST OF ABBREVIATIONS

1D	one-dimensional
2D	two-dimension
AT-III	antithrombin-III
CD	cyclodextrin
CD_3COOD-*d4*	deuterated acetic acid
CH_3OH	methanol
CiD	circular dichroism
COSY	Correlation Spectroscopy
D_2O	deuterium oxide
DMSO-*d6*	deuterated dimethyl sulfoxide
DS	degree of substitution
FDPX	fondaparinux
GAG	glycosaminoglycan
GlcA	β-D-glucuronic acid
GlcN	D-glucosamine
GlcNAc	*N*-acetylated D-glucosamine
GlcNS	*N*-sulfated D-glucosamine
HCl	hydrochloric acid
HIT	heparin-induced thrombocytopenia
HMBC	Heteronuclear Multiple-Bond Correlation
HSQC	Heteronuclear Single-Quantum Correlation
IdoA	α-L-iduronic acid
LMWH	low molecular weight heparin
mRNA	messenger ribonucleic acid
MS	mass spectrometry
MTR	mitragynine
NaOD	deuterated sodium hydroxide
NMR	nuclear magnetic resonance
NOE	Nuclear Overhauser Effect
NOESY	Nuclear Overhauser effect spectroscopy
per-6-NH2βCD	heptakis(6-deoxy-6-amino)-beta-cyclodextrin

per-6-SBEβCD	heptakis(6-sulfobutylated)-beta-cyclodextrin
REM	remdesivir
RNA	ribonucleic acid
ROESY	Rotating-frame Overhauser effect spectroscopy
SARS-CoV-2	Severe Acute Respiratory Syndrome Coronavirus 2
SBEβCD	sulfobutylated-beta-cyclodextrin
SBEγCD	sulfobutylated-gamma-cyclodextrin
SGM	sugammadex
TOCSY	Total Correlation Spectroscopy
UV-Vis	Ultraviolet-visible

INTRODUCTION

1.1. Cyclodextrins

1.1.1. The structure of cyclodextrins

Cyclodextrins (CD) are cyclic, non-reducing oligosaccharides composed of α-D-glucopyranose units. The subunits are linked by α-1,4-glycosidic bonds. The three main CDs can be distinguished by the number of the monosaccharide subunits, α-, β- and γ-cyclodextrins corresponding to 6, 7 and 8 glucose units [1]. Their schematic structure is shown in Figure 1. CDs exhibit a truncated cone-shaped surface, and their cavity size is determined by the number of α-D-glucopyranose subunits. The inner cavity of the CDs is slightly apolar due to the presence of hydrogen atoms and glycosidic oxygen bridges, whereas the outer surface is more hydrophilic. The narrower rim of the CDs possesses primary hydroxyl groups of the glucopyranose units (at position 6), while the wider rim possesses secondary hydroxyl groups at position 2 and 3. This distinction allows for the identification of narrower primary and wider secondary sides of CDs [2]. Moreover, these hydroxyl groups confer good water solubility (except for βCDs) [3].

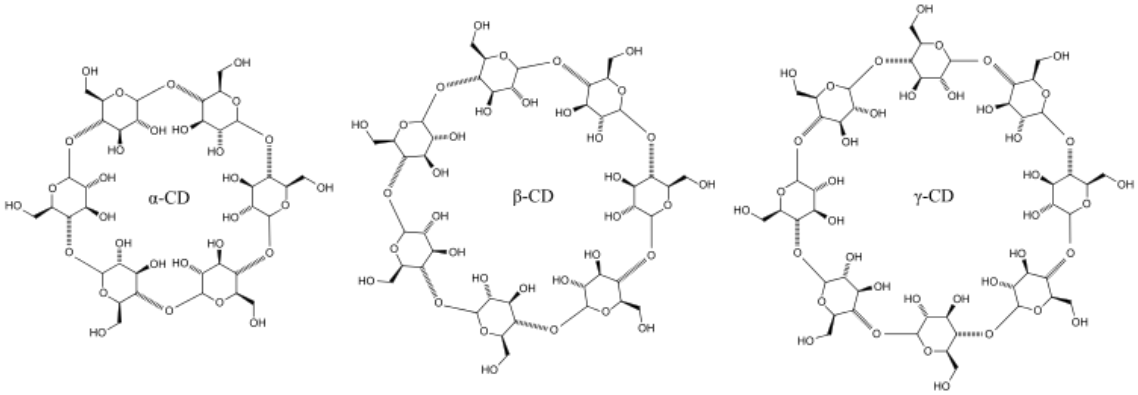

Figure 1. Schematic structure of the three main native cyclodextrins.

1.1.2. Cyclodextrin derivatives

The substitution of primary and secondary hydroxyl groups on glucopyranose units offers numerous possibilities for the preparation of various semisynthetic derivatives [4,5]. In the context of CD derivatives, the degree of substitution (DS) indicates the average number of hydroxyl groups substituted per a CD molecule. Derivatives can be

categorized based on the number of substituents (mono- or polyfunctional derivatives), the position of the substituents (persubstituted or randomly substituted derivatives), and ionizability (neutral or ionizable - positively or negatively charged derivatives). Introduction of an ionizable substituent can confer a constant or pH-dependent charge to the CD. In our work, we used native CDs as well as several β- and γCD derivatives (see Figure 2).

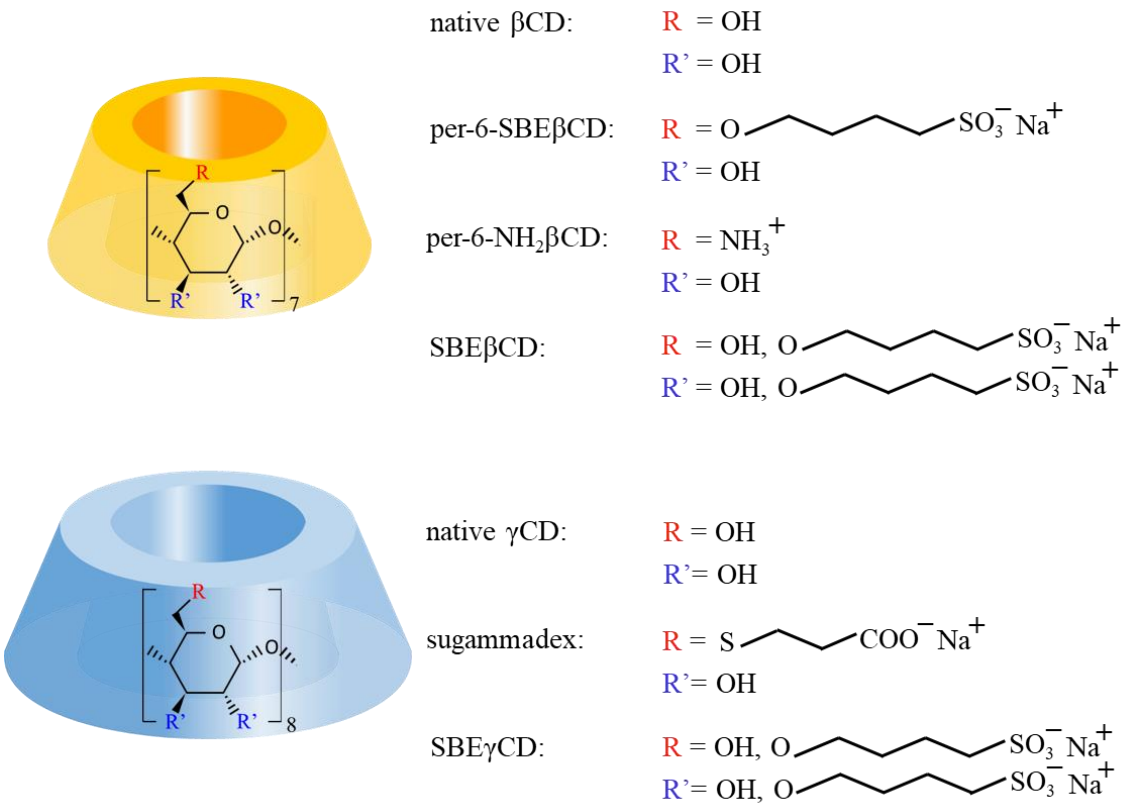

Figure 2. Structures of the β- (yellow) and γCD (blue) derivatives applied herein.

1.1.3. Complexation with cyclodextrins

CDs capable of encapsulating small apolar molecules owing to their hydrophobic, and bilaterally opened cavity. They serve as host molecules by encapsulating guest molecules with appropriate size and geometry. α-CD is suitable for complexing guests with small molecular weights, often containing aliphatic (side) chains; β-CD usually complexes aromatic and heterocyclic compounds; γ-CD can even form stable complexes with macrocycles and steroids [6]. Non-covalent interactions such as

hydrogen bonding, dipole-dipole interaction, and electrostatic interaction (in the case of ionic CD derivatives) occur between the guest and the host upon complex formation.

The formation of CD complexes could result in many beneficial consequences and the CD complexes have numerous advantageous applications. Their versatility finds use in pharmaceutical sciences, cosmetic and food industry, as well as in environmental or analytical chemistry [2,7,8]. Complexation can enhance the solubility of poorly soluble compounds [9,10] and it can change the spectral properties of the molecules, the latter phenomenon is exploited in many analytical methods [11,12]. Furthermore, the inner cavity of CDs behaves as a chiral environment as they contain several chiral centres, thus providing the possibility to separate enantiomers in capillary electrophoresis [2,13]. The different CD binding of enantiomers can lead to diastereomeric complex pairs with different apparent stability and different physical and chemical properties [14]. In order to achieve enantiomer separation, the residence time in the free and complexed form of the analyte must not be the same for the two enantiomers. In this case a difference between binding constants is necessary and the enantioseparation will be based on the same principle as in chromatographic methods. However, enantiomer separation by cyclodextrins is also possible in the case of identical complex stability of the enantiomers, as enantioseparation in this case is ensured by the different mobilities of the transient diastereomeric complexes [15]. In most cases, complexation stabilizes the guest molecule, protecting it from external influences and the concomitant degradation [16,17]. In some cases, CDs can also act as catalysts through accelerating chemical reactions [18].

Moreover, CDs could also be used in the clinical practice as selective antidotes, for example, sugammadex (Bridion®) is used in general anaesthesia to suspend the neuromuscular blockade induced by the anaesthetic muscle relaxant rocuronium and vecuronium [19]. Sugammadex is a modified γCD, persubstituted by 3-mercaptopropionic acid sidechains on its primary hydroxyl groups (Figure 1). This not only resulted in an extended cavity size but also enhances the stability of the complex through electrostatic interaction (between the negatively charged CD sidechains and the positively charged quaternary nitrogen atom of the immersed guest molecule). The stability constant of the non-covalent complex is so high that sugammadex is able to

bind the free drug molecules in the plasma irreversibly, thus reducing the concentration of the muscle relaxant and suspending its action.

1.1.4. Investigation of cyclodextrin complexes by NMR spectroscopy

Nuclear Magnetic Resonance (NMR) spectroscopy is one of the most important analytical methods that provides valuable insights into the structural and dynamic aspects of CD-complexes. NMR measurements can be used to determine spatial arrangement of the molecules, thereby providing a deeper insight into the three-dimensional structure of the complexes and the nature of the interactions between the host and guest molecules [20]. In addition, NMR spectroscopy provides not only information about the structure of the complexes but the dynamic behaviour of them [21].

1.1.4.1. Exploring complex stability through NMR spectroscopy

NMR spectroscopy stands out as one of the most versatile techniques for studying complex stability [22]. In most cases, complex stability constants are determined through calculations based on chemical shift change, as this parameter offers the highest accuracy in spectral measurement, with an uncertainty of merely ±0.005 ppm [22] achievable using high-field superconducting magnets (> 400 MHz). The increase in sensitivity due to the increasing field strength of more modern instruments, which can be further amplified with a cryoprobe, not only enables faster and/or lower concentration ^{1}H NMR titrations, but also allows the monitoring of chemical shifts of ^{13}C nuclei[23].

During the NMR titration, the concentration of the guest molecule is typically remains constant, while the concentration of CD is gradually increased. During the evaluation the chemical shift of the carbon-bonded protons of the guest molecule (δ^{G}) is recorded, and chemical shift changes ($\Delta\delta^{G}$) are calculated at each titration point. The resulting $\Delta\delta^{G}$ versus c_{CD} datasets generates titration curves, and employing nonlinear parameter estimation yields the most accurate determination of stability constants [22].

The mass-balance equations for both constituents read:

$$c_{G} = [G] + [G{\cdot}CD]$$

$$c_{CD} = [CD] + [G{\cdot}CD]$$

which can be reformulated in terms of the cumulative β association (i.e., binding or formation) constants of the complexes, yielding:

$$c_{\mathrm{G}} = [\mathrm{G}](1 + \beta_{11}[\mathrm{CD}]) \quad (1)$$

$$c_{\mathrm{CD}} = [\mathrm{CD}](1 + \beta_{11}[\mathrm{G}]) \quad (2)$$

Although stability constants acquired from the titration curves of distinct carbon-bound protons may differ slightly, simultaneous regression of these titration curves results in a more accurate constant. Stability constant between 10 and 10^4 can "easily" be determined by NMR titration as in this case the concentrations of the interacting molecules fall in the millimolar range during titration. Additionally, it is feasible to calculate the stability constant(s) using the chemical shift changes of CD alone or both reactants (CD and the guest) [23].

1.1.4.2. Characterization of complex structures through NMR spectroscopy

NMR spectroscopy provides atomic-level insights into the structure of CD complexes in solution [24].

In the case of ^{1}H NMR studies, the simplest source of structural information arises from the complexation-induced chemical shift changes ($\Delta\delta$) of individual protons. In native CDs, H3 and H5 protons are located in the apolar cavity, and a significant decrease in the chemical shift of these nuclei may suggest the inclusion of the guest molecule's electron-rich moiety within the CD cavity [25].

Similarly, a larger (absolute value) chemical shift change ($\Delta\delta$) of a certain ^{1}H signal of the guest molecule indicates a more significant role of the given molecule moiety in complex formation [25]. However, chemical shifts might also change due to indirect factors, such as spatial structure changes of the guest molecule.

More conclusive structural insight can be obtained by measuring the nuclear Overhauser effect (NOE) [26]. The NOE provides information about the spatial proximity of protons, which can even be quantitatively calibrated. The NOE is a manifestation of dipolar cross-relaxation between two non-equivalent nuclear spins that are within a close spatial distance (< 5 Å) [27]. NOE intensities are scaled with $r^{(-6)}$, where r represents the mean distance between the protons. Intermolecular NOE cross-peaks hold significant value as they indicate spatial proximity between individual protons of the

CD and the guest molecule, thereby enabling the construction of detailed geometric models. For instance, the dipolar cross-peaks involving H3 and H5 protons of the CD can be utilized to identify the specific part of the guest molecule involved in complexation, additionally in some cases even the direction of the inclusion can be determined.

The selection of pulse programs for NOE measurements is influenced by the correlation time (τ_c) of the supramolecular complex's "rotation" [26]. This means that on a 600 MHz frequency instrument (ω_0), positive NOEs are anticipated for molecules with molecular weights below ~1 kDa (fast rotation, $\omega_0 \cdot \tau_c >> 1$), while negative NOEs ($\omega_0 \cdot \tau_c << 1$) are expected only for compounds with molecular weights above 5 kDa. Since the molecular mass of 1:1 CD supramolecular complexes usually fall in the transitional range, where the NOE value is weak or even null, 1D or 2D NOESY spectra may contain limited intermolecular cross-peaks. In such cases, Rotating frame Overhauser Effect Spectroscopy (ROESY) measurements are commonly used, where NOE is consistently positive [28].

1.2. Remdesivir

Remdesivir (REM) was the first antiviral drug (Veklury™) approved by US Food and Drug Agency for the treatment of COVID-19 [29]. In December 2019, Wuhan, China, SARS-CoV-2 (Severe Acute Respiratory Syndrome Coronavirus 2) caused a severe respiratory illness that has become arguably one of the most serious health concerns that has impacted the entire world [30,31]. REM has broad antiviral activity against mRNA viruses, and it was originally developed to treat Marburg and Ebola viruses [32]. It is a monophosphoramidate prodrug (Figure 3), that is metabolically transformed by esterases and kinases into the pharmacologically active nucleoside, a triphosphate analogue. The active metabolite competes with adenosine phosphate and acts as an RNA-dependent RNA polymerase inhibitor [33]. Due to REM's high first pass liver metabolism, it cannot be applied orally [34], consequently an intravenous infusion in the form of a parenteral solution is the only approved administration route. REM is poorly soluble in water (0.028 mg/mL) therefore solubilizing excipients are required to formulate the product. At an early stage of the formulation a randomly substituted

multicomponent mixture of sulfobutylether-beta-cyclodextrin (SBEβCD, DS ~ 6.5) is used at pH 2.0 for this purpose.

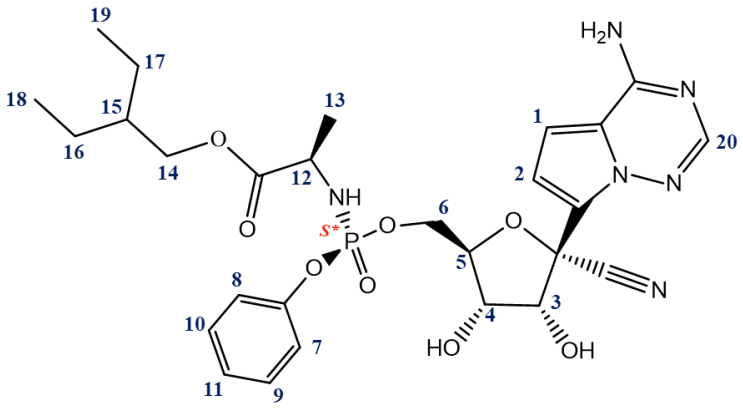

Figure 3. Chemical structure and numbering of remdesivir.

1.3. Mitragynine

Mitragynine (MTR) is the main alkaloid of *Mitragyna speciosa* [35], known as *kratom* [36]. The plant belongs to the Rubiaceae family (coffee plant family) and indigenous in Asia, mainly in Thailand and Malaysia [37]. The leaves of this evergreen tree have been used in South Asia for hundreds of years to treat a variety of illnesses. It is traditionally consumed as a tea, or the fresh leaves are chewed directly [38]. Leaves are commonly used for their stimulating and analgesic effect [39]. At low doses, the leaves are applied for their energizing effects to enhance physical tolerance, however, during the administration of high doses opioid-like effects become predominant [40]. In addition, *kratom* is also used as a substitute of opium, therefore it is a suitable agent in the treatment of opioid withdrawal symptoms [41,42]. Alkaloids of *kratom* are partial agonists at the human μ-opioid receptors. However, they act different from the classical opioids *i.e.*, morphine and heroin since the binding of MTR to the μ-opioid receptor induces activation of the G-protein-coupled signalling cascade without the activation of β-arrestin-2. The latter activation is associated with the adverse effects of opioid receptor activation *i.e.*, respiratory depression, constipation and addiction [43,44]. However, regarding the consumption of *kratom*, several withdrawal symptoms have been reported previously, such as muscle and bone pain, insomnia, anxiety, decreased appetite, or severe craving [45,46].

Nowadays the most studied alkaloid of the plant is mitragynine, which was isolated and first described by Field et al. in 1921 [47]. The molecule is a tetracyclic indole alkaloid with very poor aqueous solubility (at neutral pH), its structure is shown in Figure 4.

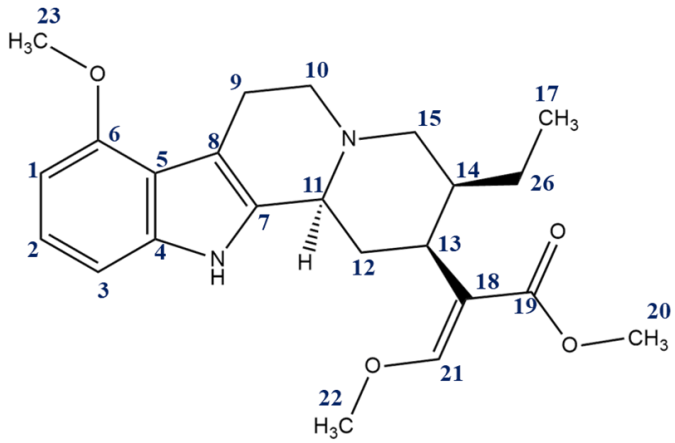

Figure 4. Chemical structure and numbering of mitragynine

1.4. Fondaparinux

Fondaparinux (FDPX) is a synthetic pentasaccharide applied in heparin-based anticoagulant therapy. It was designed to mimic the heparin pentasaccharide sequence present in each heparin-related drugs and it is essential for activating the protease inhibitor antithrombin-III (AT-III), thus enhancing its inhibitory activity toward factor Xa [48]. AT-III primarily inhibits coagulation factors IIa and Xa, making it a key inhibitor in the coagulation cascade [49].

Heparin, an anionic linear polysaccharide, was the first anticoagulant drug to bind to AT-III. It belongs to the glycosaminoglycan (GAG) family and is naturally synthesized and stored in mast cells [50]. Although the core structure of heparin consists of repeating 1,4-linked uronic acid and glucosamine disaccharides, it has a microheterogenous and polydisperse structure due to various modification of its monosaccharide subunits. The hexuronic acid is either α-L-iduronic acid (IdoA) or β-D-glucuronic acid (GlcA), which may be 2-*O*-sulfated. The hexosamine residue is D-glucosamine (GlcN), which may be sulfated at position 3-*O* and 6-*O*, and can also be *N*-sulfated (GlcNS,), *N*-acetylated (GlcNAc) or remain unmodified as a primary amine [51]. Despite its numerous undesirable side effects, heparin is a widely used anticoagulant drug in the clinical practice. However, nowadays, low molecular weight

heparins (LMWHs) have gained popularity in the anticoagulant therapy due to their predictable activity, better bioavailability, longer half-life, and enhanced safety. LMWHs are derived from unfractionated heparin through chemical or enzymatic depolymerization reactions, producing polydisperse mixtures of heparin-derived oligosaccharides [52].

In contrast to the biological products mentioned above, FDPX is a synthetic methyl glucoside analogue of the pentasaccharide sequence (Figure 5) responsible for binding to AT-III in each heparin derivative drugs [53]. It is able to bind AT-III specifically, and, within its therapeutic range, it does not interact with other proteins. During subcutaneous administration it archives nearly 100% bioavailability in healthy individuals [53]. Moreover, the half-life of FDPX is ranging from 17 to 20 hours [54]. It is mainly used for the prevention of venous thromboembolic events, as well as for the treatment of deep vein thrombosis and pulmonary embolism. Unlike heparin, which can cause heparin-induced thrombocytopenia (HIT), a life-threatening immune-driven adverse effect, FDPX does not cause HIT and can be used in patients with or suspected of having HIT[55]. However, FDPX can cause haemorrhagic complications, which can be very dangerous as its anticoagulant effect cannot be neutralize by protamine.

Protamine sulfate is commonly used in the clinical practice to neutralize the anticoagulant effect of heparin. Owing to its basic and polycationic peptide nature, it binds to the polyanionic heparin through electrostatic interactions, forming an inactive complex devoid of anticoagulant properties [56]. Unfortunately, protamine is unable to suspend the anticoagulant function of LMWHs and is even less effective in the case of FDPX. Consequently, the search for new antidotes is essential, particularly ones that could be suitable for all heparin derivatives [57]. Modified carbohydrates and cyclodextrins emerge as promising candidate antidotes among the various core structures [58].

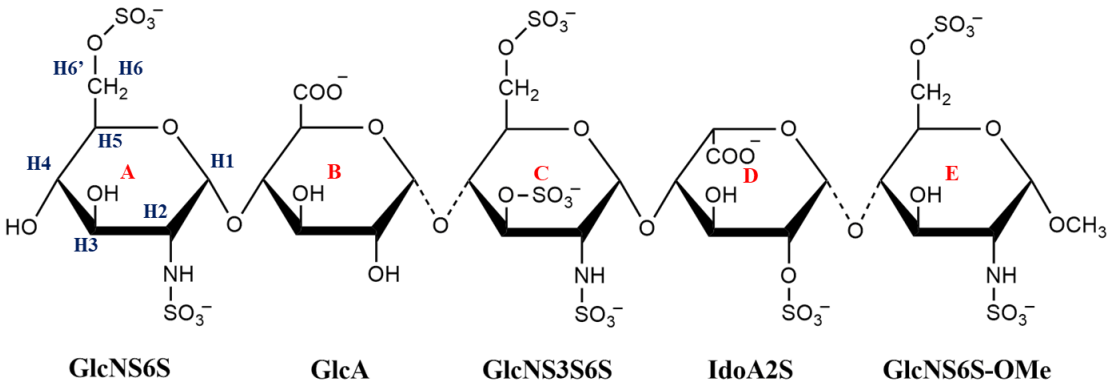

Figure 5. Chemical structures and numbering of fondaparinux along with the abbreviation of the subunits.

OBJECTIVES

The main aim of this work was to investigate various cyclodextrin complexes of three drug molecules i.e., the antiviral REM, the *kratom* alkaloid MTR and the anticoagulant FDPX by extensive ^{1}H and 2D NMR experiments. We aimed to gain molecular level information (i.e., to determine the stoichiometry of association, the stability constants, and the structure of the formed complexes) about the supramolecular systems.

Our objective was to characterize charge-dependent molecular encapsulation of REM using various β- and γCD derivatives (βCD, per6-SBEβCD, SBEβCD, γCD, SBEγCD and sugammadex). Since there was no experimentally available literature data on the pK_a value of REM, our goal was to experimentally determine the pK_a of the molecule, in order to better understand its charge-dependent behaviour.

Additionally, we aimed to understand the inclusion complex formation between MTR and SBEβCD. Specifically, our aim was to investigate how the sulfobutylation of βCD impacts the complexation of MTR.

The present study aims to characterize the molecular interactions between the polyanionic FDPX and the polycationic cyclodextrin per6-NH_2-βCD. Moreover, the stabilizing effect of the per6-NH_2-βCD on FDPX degradation under acidic conditions was also investigated. Our aim here was to gain a deeper insight into the mechanism of the degradation of FDPX.

METHODS

1.5. Chemicals

Both native CDs (βCD, γCD) and CD derivatives - i.e., randomly substituted SBEβCD (DS ~ 6.5), SBEγCD (DS ~ 5.7) and single isomer sugammadex (SGM) [19], per-6-amino-βCD (per-6-NH_2βCD) and per-6-sulfobutylated-βCD (per-6-SBEβCD [59] were products of CycloLab Ltd. (Budapest, Hungary).

Remdesivir was purchased from Echemi Pharma, Qingdao, China. Mitragynine was isolated and purified by centrifugal partition chromatography from *kratom* extract and it was a gift of RotaChrom Ltd, Hungary. Fondaparinux was isolated from Arixtra® 2.5mg/0.5mL injections. Briefly, ten prefilled injections were combined and subjected to dialysis (Spectra/Por® dialysis membrane – Biotech- CE Tubing MWCO: 100-500 Da) against deionized water for three consecutive days. Thereafter, the dialysate was subjected to freeze-drying.

Deuterated solvents for NMR measurements were purchased from several sources: D_2O (99.9 atom% D) and DMSO-*d6* (99.9 atom% D) were obtained from Merck (Darmstadt, Germany), while deuterated acetic acid-*d4* (CD_3COOD-*d4*) was purchased from Cambridge Isotope Laboratories Inc (Tewksbury, Massachusetts, US). Other base chemicals of analytical grade were from commercial suppliers and were used without further purification.

1.6. NMR methods

NMR spectroscopy measurements were carried out on a 600 MHz Varian DDR NMR spectrometer (Agilent Technologies, Palo Alto, CA, USA), equipped with a 5 mm inverse-detection probehead and a pulsed-field gradient module. Standard pulse sequences and processing routines available in VnmrJ 3.2C/Chempack 5.1 and MestreNova 14.2.0 were used. The complete resonance assignments of the investigated chemicals were established from direct ^{1}H-^{13}C, long-range ^{1}H-^{13}C, and scalar spin-spin connectivities derived from one-dimensional (1D) ^{1}H, two-dimensional (2D) ^{1}H-^{1}H gCOSY, zTOCSY (mixing time of 150 ms), ROESYAD and NOESY (in both cases mixing time from 250 and 400 ms were used), ^{1}H-^{13}C gHSQCAD ($^{1}J_{CH}$ = 140 Hz -

based on the one bond heteronuclear coupling constant) and gHMBCAD ($^{n}J_{CH}$ = 8 Hz - based on the optimized long-range proton–carbon coupling constant) experiments.
Additional NMR studies were performed on an 800 MHz Bruker Avance III HDX 800 MHz spectrometer equipped with a 5 mm $^{1}H/^{13}C/^{15}N$ Triple Resonance ^{13}C Enhanced Salt Tolerant Cold Probe (^{1}H: 799.7 MHz, ^{13}C: 201.0 MHz), controlled by the TopSpin 3.5 pl 7 software (Bruker Biospin GmbH, Rheinstetten, Germany).
The ^{1}H chemical shifts were referenced to the methyl singlet (δ = 3.31 ppm) of internal methanol (CH_3OH), a reference substance without any possible interaction with the CD.
All NMR spectra were acquired in standard 5 mm NMR tubes at 25 °C.

1.6.1. ^{1}H NMR titration experiments

Different conditions were used during sample preparation regarding the three different drug molecules, due to their characteristic properties (e.g., different solubility, stability). Following methods were applied:
REM containing samples were prepared in acidic (D_2O, HCl; pH 2.0) media, due to its poor water solubility.
As for MTR, all samples were prepared in an acetate buffer, where the pH of 20 mM CD_3COOD-*d4* solution in D_2O was adjusted with NaOD to pH 4.5.
In the case of FDPX samples, complex formation was investigated under two different circumstances. Aqueous samples were prepared in 0.1 M phosphate buffers of pD 2.0 and pD 7.4.

1.6.1.1. Determination of the complex stoichiometry

The stoichiometry of the formed complexes of three drug molecules (D) with various CDs was investigated based on Job's method of continuous variation [60]. All spectra were recorded at 25 °C. The total molar concentration of the host and guest components $c_D + c_{CD}$ was kept constant (in case of REM and MTR at 1 mM and in the case of FDPX at 3 mM), while the mole fraction of the drug $c_D = \frac{c_D}{c_D + c_{CD}}$ was varied gradually in 0.1 unit steps from 0 to 1. ^{1}H chemical shifts δ^D were recorded for several drug resonances and complexation-induced displacement values $\Delta\delta^D = |\delta^D - \delta_D|$ were calculated with respect to δ_D measured in the absence of CD. To construct Job's plots,

$\Delta\delta^{\mathrm{D}}$ values were multiplied by the mole fraction of the D and depicted as a function of x_{D}.

1.6.1.2. Determination of the stability constant

To determine the apparent and averaged (latter in the case of the randomly substituted CD derivatives) stability constant in each case, separate ^{1}H NMR titrations were performed on the 3 drug molecules. Owing to the fact, that the experimental design underlying Job's plots may not be optimal to determine the stability constants of the formed complexes [22], separate NMR titrations were needed to be performed, under the same experimental conditions as written in *Chapter 3.2.1.* ^{1}H NMR spectra were recorded in each titration step at 600 MHz and 25 °C after equilibration of the prepared samples.

^{1}H NMR titration of remdesivir

For each βCD derivatives and in case of some γCD derivatives 500 µL 1 mM REM was titrated with increasing portions (5 to 1000 µL) of CD stock solutions (10 mM βCD, 6.16 mM SBEβCD, 9.05 mM per-6-SBEβCD, 11.45 mM γCD, 6.16 mM SBEγCD) while in the case of the native γCD 500 µL 0.45 mM REM was titrated with 10 mM γCD. Due to the poor solubility of SGM, the conditions were changed as follows: 500 µL of 0.2 mM REM solution was titrated with 5 to 600 µL of 0.66 mM SGM stock solution. All titration datasets were analysed by the following method. The experimental titration curves for well-resolved resonances of the REM were evaluated by the Origin 2017 software (OriginLab, Northampton, MA, US), using the 1:1 REM·CD complex as confirmed earlier by the Job's method. If complexation occurs with rapid kinetics on the NMR chemical shift timescale, the observed chemical shift $\delta^{\mathrm{obs}}_{\mathrm{REM,i}}$ of the *i*th carbon-bound proton in REM becomes a mole-fraction weighted average of the species-specific values in the uncomplexed REM ($\delta^{\mathrm{REM,i}}$) and in the complex ($\delta^{\mathrm{REM\cdot CD,i}}$),

$$\delta^{\mathrm{obs}}_{\mathrm{REM,i}} = \frac{\delta^{\mathrm{REM,i}} \cdot c_{\mathrm{REM}} + \delta^{\mathrm{REM\cdot CD,i}} \cdot c_{\mathrm{REM\cdot CD}}}{c^{\mathrm{REM}}_{\mathrm{total}}} \qquad (3)$$

where c_{CD} and c_{REM} denote equilibrium concentrations, while $c_{\mathrm{total}}^{\mathrm{CD}}$ and $c_{\mathrm{total}}^{\mathrm{REM}}$ are the total concentrations of the compounds in the solution [22].

The mass-balance equation for REM read:

$$c_{\mathrm{REM}} = [\mathrm{REM}] + [\mathrm{REM{\cdot}CD}] \qquad (4)$$

which can be reformulated in terms of the *K* association (i.e., binding or formation) constants of the complex, yielding:

$$c_{\mathrm{REM}} = [\mathrm{REM}](1 + K_1[\mathrm{CD}]) \qquad (5)$$

Chemical shifts for all hydrogens (*i*) of REM were plotted as a function of V_{CD} (μL) to select the resonances with sufficient sensitivity ($\Delta\delta$) to enter the evaluation. The selected datasets were fitted to the model described above, to determine the apparent complex stability constant (log*K*) values.

^{1}H NMR titration of mitragynine

For the native βCD, 500 μL 1 mM MTR was titrated with increasing portions (5-1000 μL) of 10 mM βCD stock solution, while in the case of SBEβCD 500 μL 1.05 mM MTR was titrated with 9.88 mM SBβCD. The experimental titration curves for well-resolved resonances of MTR (and for βCD, that of its H3 proton) were simultaneously evaluated by the OPIUM software [61].

In the case of βCD, the nonlinear titration fitting was performed by assuming the formation of a single MTR·βCD (1:1) complex, as it was mentioned above in the case of REM. In contrast, the titration curves with SBEβCD were fitted based on the principles summarized here by assuming the formation of both MTR·CD and 2MTR·CD complexes. Since the complex formation occurs with rapid kinetics, the chemical shifts of the observed signals become a mole-fraction weighted average: uncomplexed MTR ($\delta^{\mathrm{MTR,i}}$) and the complexes ($\delta^{\mathrm{MTR{\cdot}CD,i}}$), ($\delta^{2\mathrm{MTR{\cdot}CD,i}}$),

$$\delta_{\mathrm{MTR},i}^{\mathrm{obs}} = \frac{[\mathrm{MTR}]\delta^{\mathrm{MTR},i} + [\mathrm{MTR{\cdot}CD}]\delta^{\mathrm{MTR{\cdot}CD},i} + 2[2\mathrm{MTR{\cdot}CD}]\delta^{2\mathrm{MTR{\cdot}CD},i}}{c_{\mathrm{MTR}}} \qquad (6)$$

where square brackets denote equilibrium concentrations. Analogously defined intrinsic chemical shifts ($\delta^{\mathrm{CD,j}}$, $\delta^{\mathrm{MTR\cdot CD,j}}$, $\delta^{\mathrm{2MTR\cdot CD,j}}$) and resonance signal averaging apply for the *j*th carbon-bound proton of the cyclodextrin:

$$\delta_{\mathrm{CD},j}^{\mathrm{obs}} = \frac{[\mathrm{CD}]\delta^{\mathrm{CD},j} + [\mathrm{MTR\cdot CD}]\delta^{\mathrm{MTR\cdot CD},j} + [\mathrm{2MTR\cdot CD}]\delta^{\mathrm{2MTR\cdot CD},j}}{c_{\mathrm{CD}}} \qquad (7)$$

The mass-balance equations for both constituents read:

$$c_{\mathrm{MTR}} = [\mathrm{MTR}] + [\mathrm{MTR\cdot CD}] + 2[\mathrm{2MTR\cdot CD}] \qquad (8)$$

$$c_{\mathrm{CD}} = [\mathrm{CD}] + [\mathrm{MTR\cdot CD}] + [\mathrm{2MTR\cdot CD}] \qquad (9)$$

which can be reformulated in terms of the cumulative β association (i.e., binding or formation) constants of the complexes, yielding:

$$c_{\mathrm{MTR}} = [\mathrm{MTR}](1 + \beta_{11}[\mathrm{CD}] + 2\beta_{21}[\mathrm{MTR}][\mathrm{CD}]) \qquad (10)$$

$$c_{\mathrm{CD}} = [\mathrm{CD}](1 + \beta_{11}[\mathrm{MTR}] + \beta_{21}[\mathrm{MTR}]^2) \qquad (11)$$

Based on the known total concentrations c_{MTR} and $c_{\mathrm{CD}}$for each titration step as well as initial guesses of the β stability constants, the OPIUM program solved the nonlinear system of equations *(10)* and *(11)* for the variables [MTR] and [CD]. These speciation calculations were integrated into a simultaneous least-squares fitting procedure of equations *(6)* or *(7)* to the measured datasets in order to iteratively refine the stability constants. From the resulting complex stability constants, the Microsoft Excel program (and for SBEβCD, also the Hyss software [62]) was used to generate the fitted NMR titration curves and the species distribution plots.

^{1}H NMR titration of fondaparinux

At pD 7.4, increasing portions ranging from 20 to 280 µL of 20.1 mM per-6-NH_2-βCD solution were added to 600 µL of 3.4 mM FDPX solution residing in the NMR tube. While at pD 2.0, 600 µL of 3.18 mM FDPX solution was titrated with 10 to 250 µL of 20.9 mM per-6-NH_2-βCD stock solution. Experimental titration curves for well-resolved resonances of FDPX and CD were evaluated by the OPIUM software by

assuming the formation of both FDPX·CD and FDPX·2CD. In case of the complex formation between FDPX and per-6-NH_2-βCD, uncomplexed FDPX (δ^i_{FDPX}) and complexed ($\delta^i_{\mathrm{FDPX{\cdot}CD}}$ and $\delta^i_{\mathrm{FDPX{\cdot}2CD}}$) species occurred in the aqueous solution,

$$\delta^{\mathrm{FDPX},i} = \frac{[\mathrm{FDPX}]\delta^i_{\mathrm{FDPX}} + [\mathrm{FDPX{\cdot}CD}]\delta^i_{\mathrm{FDPX{\cdot}CD}} + [\mathrm{FDPX{\cdot}2CD}]\delta^i_{\mathrm{FDPX{\cdot}2CD}}}{c_{\mathrm{FDPX}}} \qquad (12)$$

Analogously defined intrinsic chemical shifts (δ^j_{CD}, $\delta^j_{\mathrm{FDPX{\cdot}CD}}$, $\delta^j_{\mathrm{FDPX{\cdot}2CD}}$) and resonance signal averaging apply for any carbon-bound proton of the CD:

$$\delta^{\mathrm{CD},j} = \frac{[\mathrm{CD}]\delta^j_{\mathrm{CD}} + [\mathrm{FDPX{\cdot}CD}]\delta^j_{\mathrm{FDPX{\cdot}CD}} + 2[\mathrm{FDPX{\cdot}2CD}]\delta^j_{\mathrm{FDPX{\cdot}2CD}}}{c_{\mathrm{CD}}} \qquad (13)$$

The mass-balance equations for both constituents are:

$$c_{\mathrm{FDPX}} = [\mathrm{FDPX}] + [\mathrm{FDPX{\cdot}CD}] + [\mathrm{FDPX{\cdot}2CD}] \qquad (14)$$

$$c_{\mathrm{CD}} = [\mathrm{CD}] + [\mathrm{FDPX{\cdot}CD}] + 2[\mathrm{FDPX{\cdot}2CD}] \qquad (15)$$

Reformulation in terms of the β association constants of the complexes yields:

$$c_{\mathrm{FDPX}} = [\mathrm{FDPX}](1 + \beta_{11}[\mathrm{CD}] + \beta_{12}[\mathrm{CD}]^2) \qquad (16)$$

$$c_{\mathrm{CD}} = [\mathrm{CD}](1 + \beta_{11}[\mathrm{FDPX}] + 2\beta_{12}[\mathrm{FDPX}][\mathrm{CD}]) \qquad (17)$$

Based on the input values of c_{FDPX} and c_{CD} for each titration point (the ratio of which was checked from non-overlapping ^{1}H NMR integrals of the components) as well as initial guesses of the β stability constants, the OPIUM program solved equations mentioned for the variables [FDPX] and [CD], in order to iteratively refine the stability constants. Since the OPIUM program lacks a graphical output, the resulting equilibrium constants were used to compute species distribution data covering the 0 to 2.7 interval of the $\frac{c_{\mathrm{CD}}}{c_{\mathrm{FDPX}}}$ ratio by the ORCHESTRA program [63]. These datasets were subsequently imported into Microsoft Excel 2002, where equations *(12)* and *(13)* were used to

calculate and depict the continuous curves fitted to the experimental ^{1}H NMR titration datasets.

1.6.2. Structural studies on complex formation

To explore the spatial arrangement of the host-guest complexes and identify the interacting molecular sequences, nuclear Overhauser effect (NOE) type experiments were performed on different molar ratio drug-cyclodextrin samples at 25 °C.

2D ROESY spectra were acquired on a 600 MHz instrument, collecting 16 and 32 scans on 1258·512 data points and applying mixing times of 300 and 400 ms. In the case of FDPX samples 2D NOESY spectra were also recorded on the 800 MHz instrument, collecting 24 scans on 4096·512 data points, applying mixing times of 350 ms, 400 ms, 500 ms and 650 ms along with a 250-μW presaturation on the HDO signal for D1=2.5 s.

1.6.3. NMR investigations of FDPX degradation

To determine the structure of the FDPX decomposition product, ^{1}H and several 2D (^{1}H-^{1}H COSY, TOCSY, HSQC and ROESY) NMR spectra were recorded at 600 MHz with the same parameters described in above (*Chapter 3.2.1*). For this experiment, 5 mM FDPX was dissolved in a 0.1 M phosphate buffered D_2O at pD 2.0.

During the stability investigation, FDPX·per-6-NH_2-βCD samples with 1:0, 2:1 and 1:1 molar ratio was tested. All samples were dissolved in 0.1 M phosphate buffered D_2O at pD 2.0. In the case of the first set of experiments, ^{1}H NMR spectra of the freshly prepared samples were recorded. After keeping these samples at 25 °C for a week, their ^{1}H NMR spectra were recorded again. A second experiment was carried out to perform an accelerated decomposition investigation. ^{1}H NMR spectra of the fresh samples were recorded at 25 °C, then samples were incubated at 60 °C for 14 hours. Afterwards all samples were cooled down to 25 °C again and ^{1}H spectra were re-recorded.

1.7. UV-pH titration experiments

In the case of REM, 500 mL stock solution was prepared by dissolving the appropriate amount of Na_2HPO_4 (15.0 mM) and HCO_2NH_4 (20 mM). The desired pH values ranging from 1.75 to 5.26 (14 individual samples) were adjusted by 6.0 M HCl and 6.0

M NaOH (pH was controlled by a Metrohm 913 pH meter combined with a standard glass electrode). Thereafter, 30 μL 15 mM REM DMSO stock solution was added to each 10 mL portion of the buffered samples at a given pH, while 30 μL of DMSO were used in case of the blank solutions. UV-Vis spectra were recorded in the 220–400 nm range on a Unicam UV2 UV/Vis Spectrometer at room temperature. The whole matrix of measured absorbances in the range of 227-345 nm (typically, 590 wavelengths at each pH values) was involved in the computer evaluation using nonlinear regression as mentioned in the literature [64] by the OPIUM program to yield the pK_a of REM.

RESULTS

1.8. Remdesivir

1.8.1. Determination of the pK_a value of REM by UV-pH titration method

Based on our observations, REM solubility significantly increases below pH 3.5, suggesting that protonation may occur in this region. Interestingly in reference [65], the predicted pK_a value of REM (pK_a 0.65) seems rather low, however the site of protonation is presumably the rare, yet basic aminopyrrolo-triazin moiety. As the aminopyrrolo-triazin part is the strongest chromophore of REM, the protonation of REM evokes an intense pH-dependent spectral shift. Consequently, UV-pH titration is an appropriate choice to provide a reliable pK_a value. Figure 6 shows the registered UV absorption spectra of REM at various pH values. To determine the exact pK_a value, the whole matrix of measured absorbances was involved in the evaluation, titration curves were fitted simultaneously for all wavelengths (see inset of Figure 6), thus this evaluation yielded pK_a = 3.56 with an estimated standard deviation of 0.01.

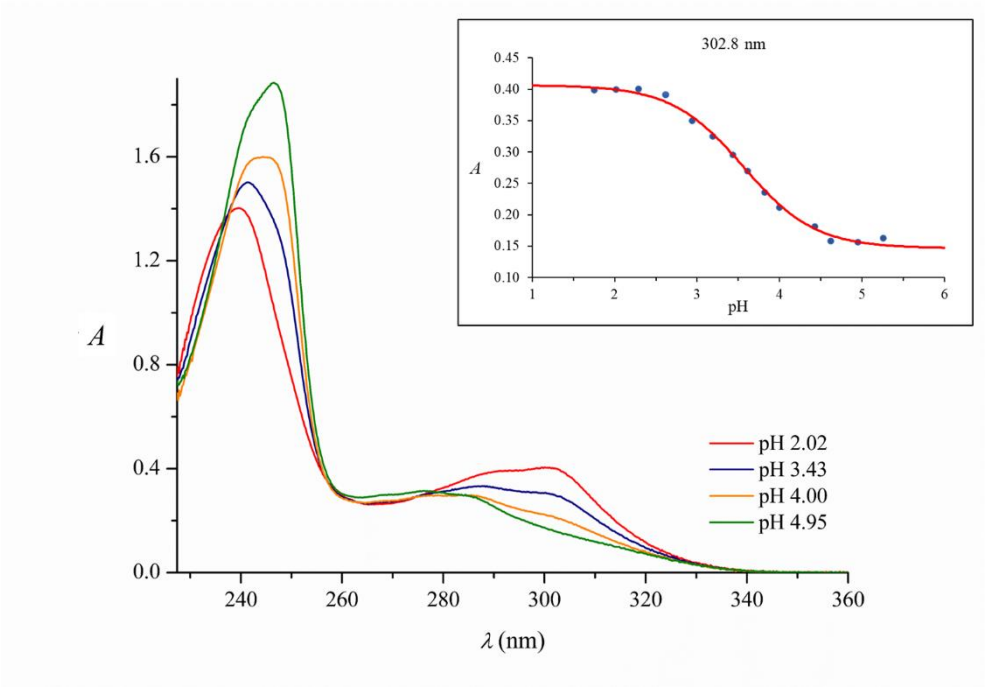

Figure 6. UV absorption spectra of REM recorded at different pH values and the titration curve at 302 nm, fitted simultaneously for each registered wavelength.

1.8.2. Stoichiometry and stability constants of various REM-CD complexes

The complex stoichiometry and stability for all six CD-REM systems were assessed by NMR spectroscopy. The complete resonance assignments of REM can be found in Table 1.

Table 1. Complete ^{1}H NMR resonance assignment for remdesivir in D_2O at pH 2.0 (600 MHz, ref. MeOH δ_H = 3.31 ppm).

No.	*^{1}H*
1	7.00 (d, *J* = 4.9 Hz, 1H)
2	7.23 (d, *J* = 4.9 Hz, 1H)
3	4.87 (m, 1H)
4	4.42 (m, 1H)
5	4.52 (m, 1H)
6	4.24 (m 1H)
6'	4.38 (m, 1H)
7-8	6.88 (d, *J* = 8.0 Hz, 2H)
9-10	7.28 (t, *J* =7.8 Hz, 2H)
11	7.18 (t, *J* =7.5 Hz, 2H)
12	3.69 (m, 1H)
13	1.26 (d, *J* = 7.4, 3H)
14	3.94 (dd, *J* = 10.8 Hz, 5.7 Hz, 1H)
14'	4.01 (dd, *J* = 10.8 Hz, 5.7 Hz, 1H)
15	1.45 (m, 4H)
16-17	1.25 (m, 4H)
18-19	0.80 (t, *J* = 7.5 Hz, 6H)
20	7.95 (s, 1H)

The most sensitive (showing the largest complexation induced chemical shift changes), non-overlapping and well-separated ^{1}H NMR resonances of REM were monitored only during different titrations. In the case of βCD, Job's plot curves (Figure 7) show a maximum at x = 0.5. Similarly, Job's experiments were performed with the other CD derivatives (data not shown) confirming 0.5 maxima in each case.

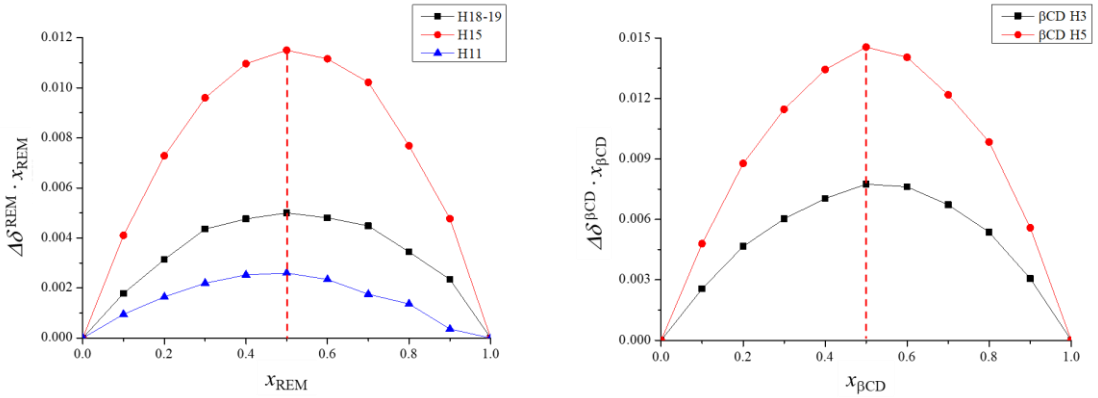

Figure 7. Job's plot for the selected ^{1}H resonances of REM (left) and βCD (right) both showing maximum at 0.5, that suggest 1:1 molar ratio for the complex in aqueous solution at pH 2.0.

To determine the stability constants of CD-REM complexes, single-tube ^{1}H NMR titrations were carried out in all cases. During the titration of REM with βCD, chemical shift variation of the following REM resonances was monitored: H1, H2, H7-8, H9-10, H11, H13, H15, H18-19 (Figure 8A). To extract a robust and reliable stability constant all eight datasets were subjected to a simultaneous nonlinear regression using Origin software (Figure 8B). This global evaluation yielded a log$K$ = 3.06 with an estimated standard deviation of 0.01. All the other obtained stability values of the various CD-REM complexes are summarized in Table 2.

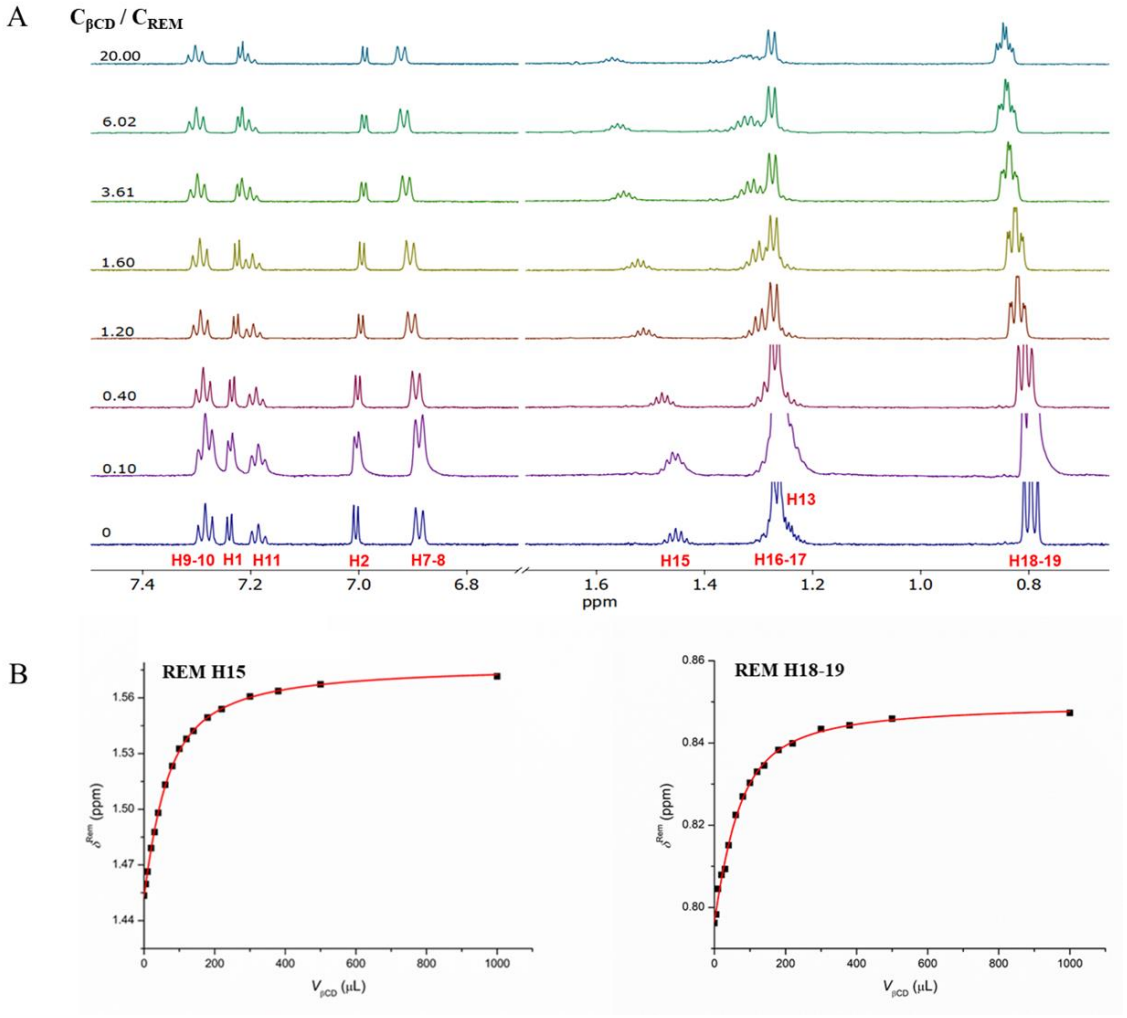

Figure 8. Representative ^{1}H NMR chemical shift changes of REM (subplot A) upon titration with βCD. Subplot B shows the selected titration profiles of REM H18–19 and H15, simultaneously fitted by the 1:1 complexation model using Origin program.

Table 2. Stability constant values of the investigated CD-REM complexes, determined by Origin software.

	βCD	***γCD***	***SBEβCD*** *(DS ~ 6.5)*	***SBEγCD*** *(DS ~ 5.7)*	***per-6-SBEβCD*** *(DS = 8.0)*	***sugammadex*** *(DS = 7.0)*
log*K*	3.06 ± 0.01	2.08 ± 0.02	3.99 ± 0.02*	2.70 ± 0.01*	4.35 ± 0.03	3.65 ± 0.04

*apparent stability constants due to the heterogeneous nature of the cyclodextrin

1.8.3. Structural characterization of various REM-CD complexes

To obtain atomic-level information on the 3D structure of the complexes 2D ROESY NMR experiments were carried out at various host-guest molar ratios. In the case of βCD 2D ROESY spectrum was registered on a 1:3 (REM-βCD) system in order to ensure significant excess of the host. Intermolecular cross-peaks could be detected between the REM's methyl- (H18-19), the methylene- (H16-H17) and the inner cavity resonances of βCD (H3 and H5) in Figure 9.

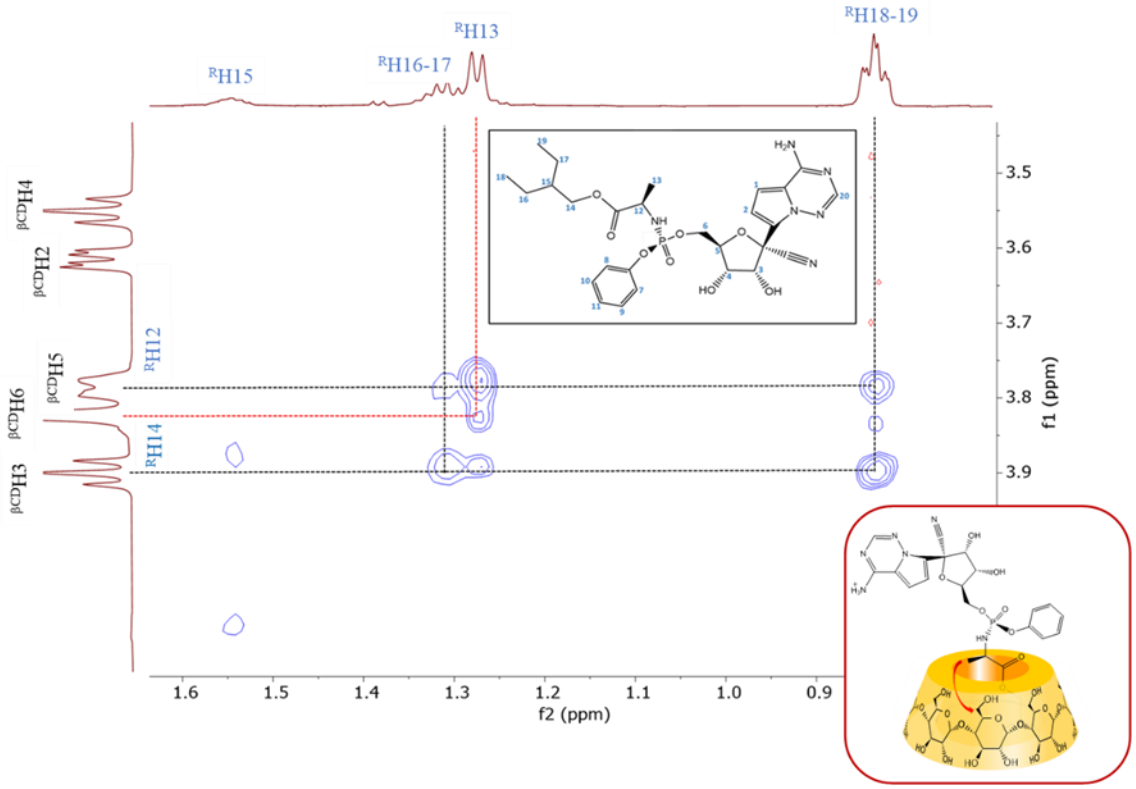

Figure 9. Partial 2D ROESY spectrum of a 1:3 molar ratio (REM-βCD) sample and the structure of the suggested inclusion complex.

The single isomeric nature and the concomitant simplicity of the NMR resonances of per-6-SBEβCD permitted the depiction of the spatial arrangement of REM-per-6-SBEβCD complex. 2D ROESY cross-peaks were detected between REM H13 and the H6 resonance of per-6-SBEβCD, besides cross-peaks between the aliphatic sidechain of REM and the inner cavity of per-6-SBEβCD (Figure 10).

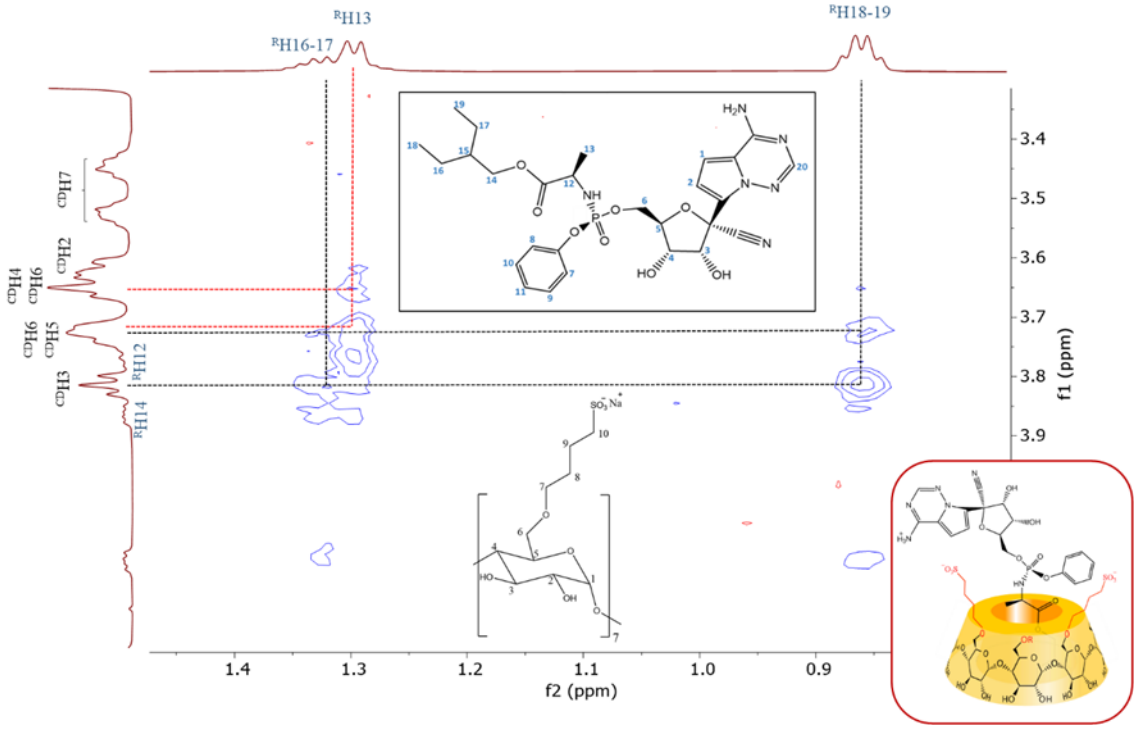

Figure 10. 2D ROESY spectrum of the 1:1 REM-per-6-SBEβCD molar ratio sample and the suggested complex geometry.

Similarly to previous observations ROESY cross-peaks could be detected between the methyl- (H18-H19) and the methylene (H16-H17) resonances as well as the methine CH signals (H15) and the H3 resonance of the SBEβCD (Figure 11). The host-guest type interaction was also confirmed by a further ROESY cross-peak between REM's H13 proton and the methylenes of the CD's sulfobutyl sidechain (Figure 11).

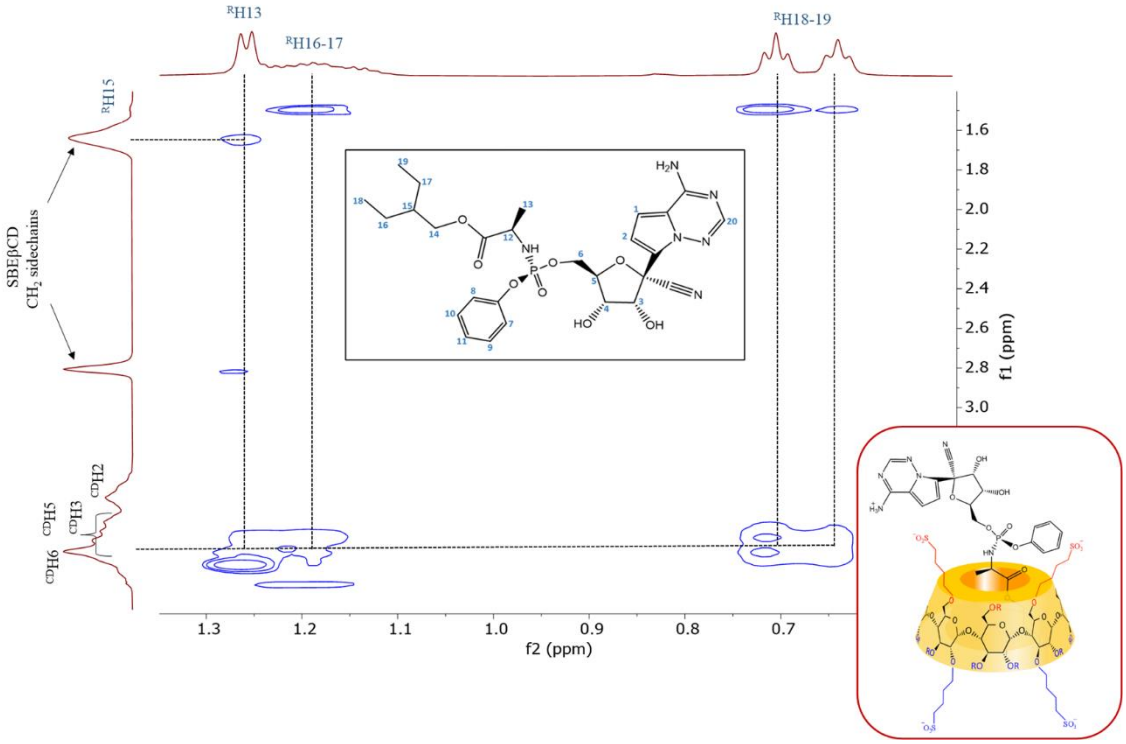

Figure 11. Partial 2D ROESY spectrum of the 1:3 REM-SBEβCD molar ratio sample along with the structure of the suggested inclusion complex.

The larger cavity of γCD is not perfectly suited for the ethylbutyl moiety, however in this case spatial proximities between the phenoxy moiety (H9-10, H11, H7-8) and the CD's inner cavity hydrogens were identified as cross-peaks. Insets of the registered 2D ROESY spectrum are shown in Figure 12.

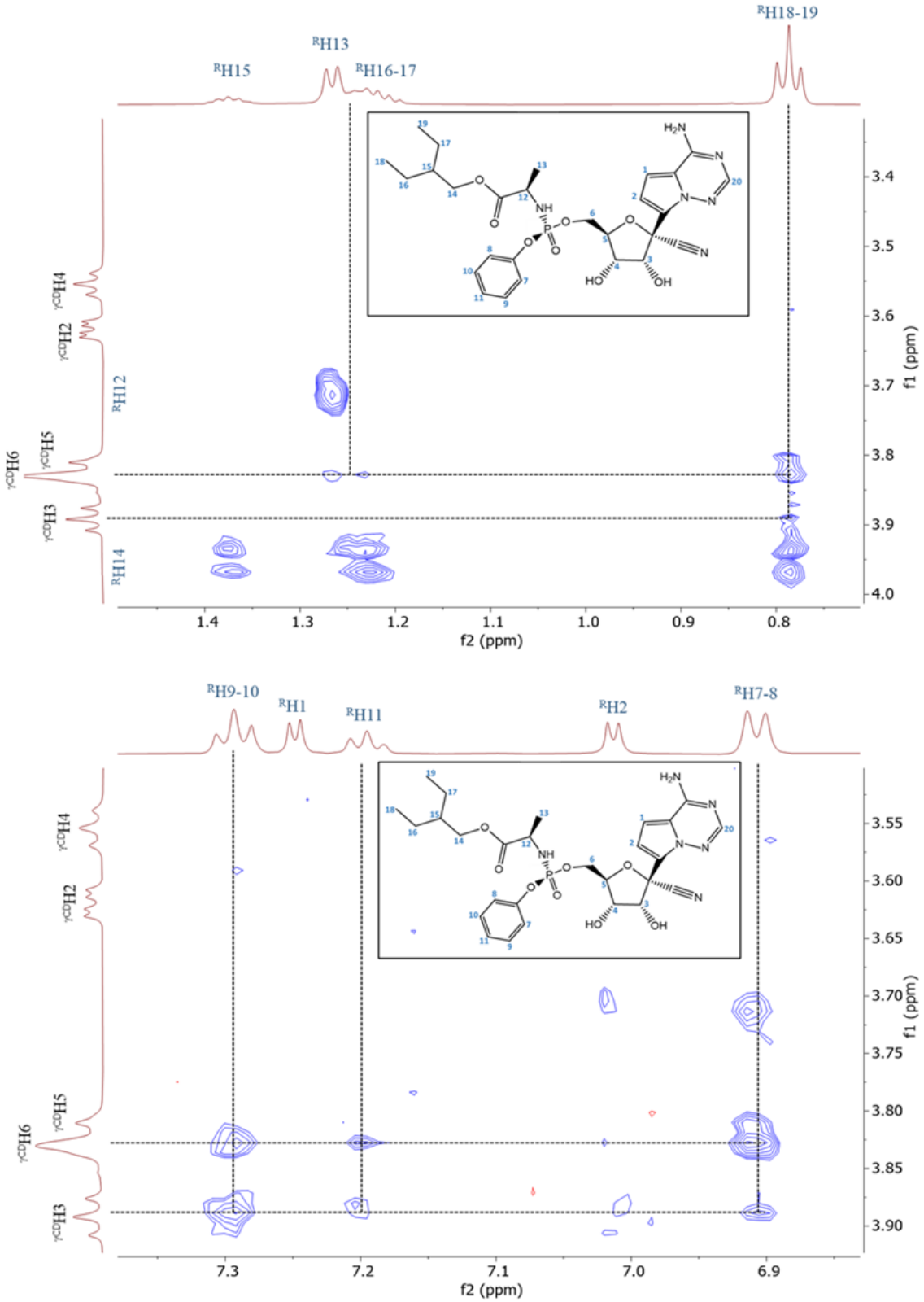

Figure 12. Partial 2D ROESY spectra of the 1:3 REM-γCD molar ratio sample.

In the case of SBEγCD based on the observed cross-peaks in the ROESY spectrum both aliphatic and aromatic parts of REM are involved in the inclusion-type complexation (see Figure 13).

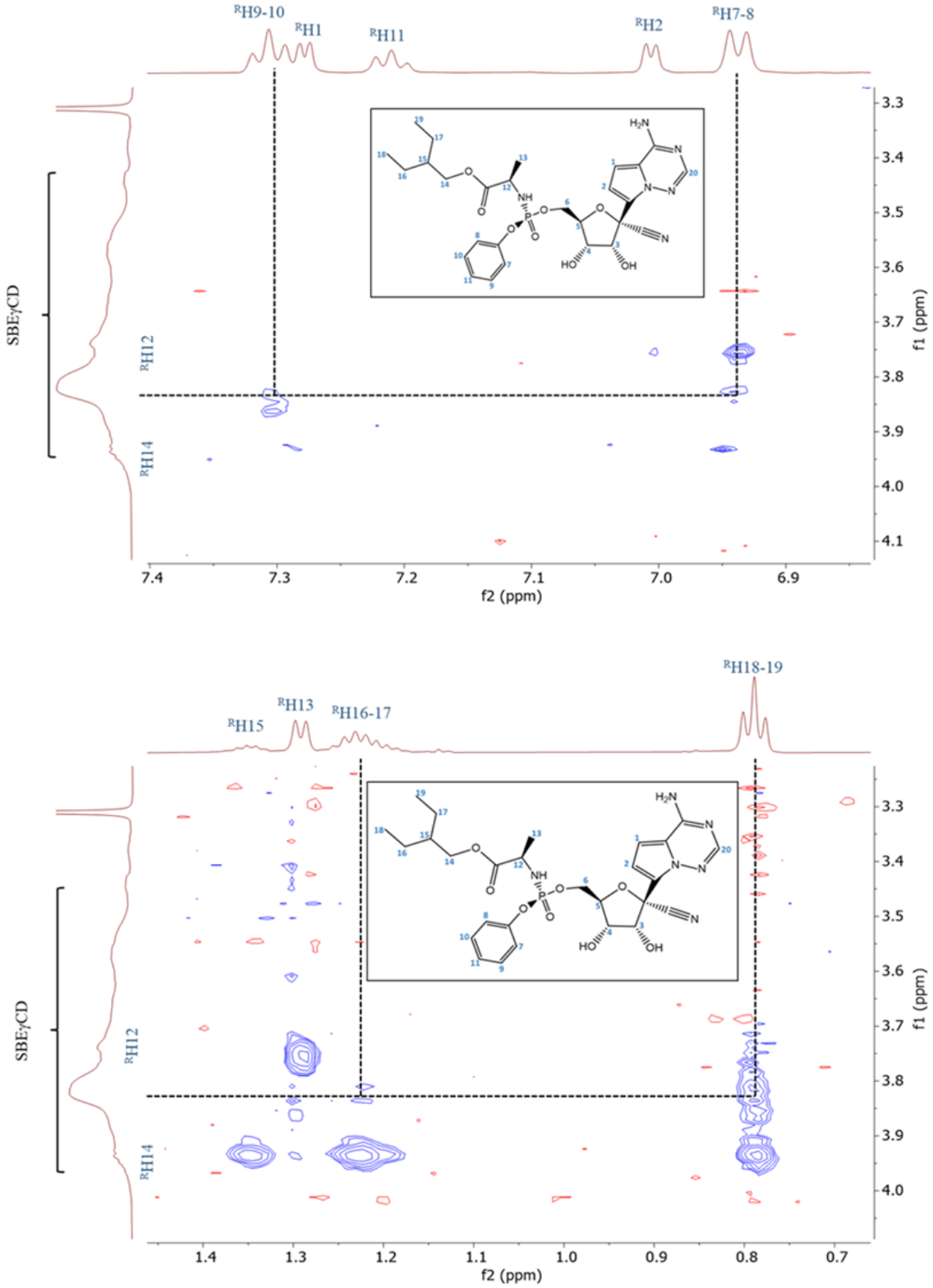

Figure 13. Partial 2D ROESY spectra of the 1:3 REM-SBEγCD molar ratio sample.

Characterization of sugammadex-REM complexation was also determined at pH 2.0 by using 2D ROESY NMR data (Figure 14). Intermolecular cross-peaks between the phenoxy moiety (H7-8 and H9-10) and the sugammadex's cavity (H3 and H5) were identified. Additionally, weak interactions could be deduced between the methyl resonances of ethylbutyl-sidechain of REM (H18-19) and those of the cavity protons (H3 and H5).

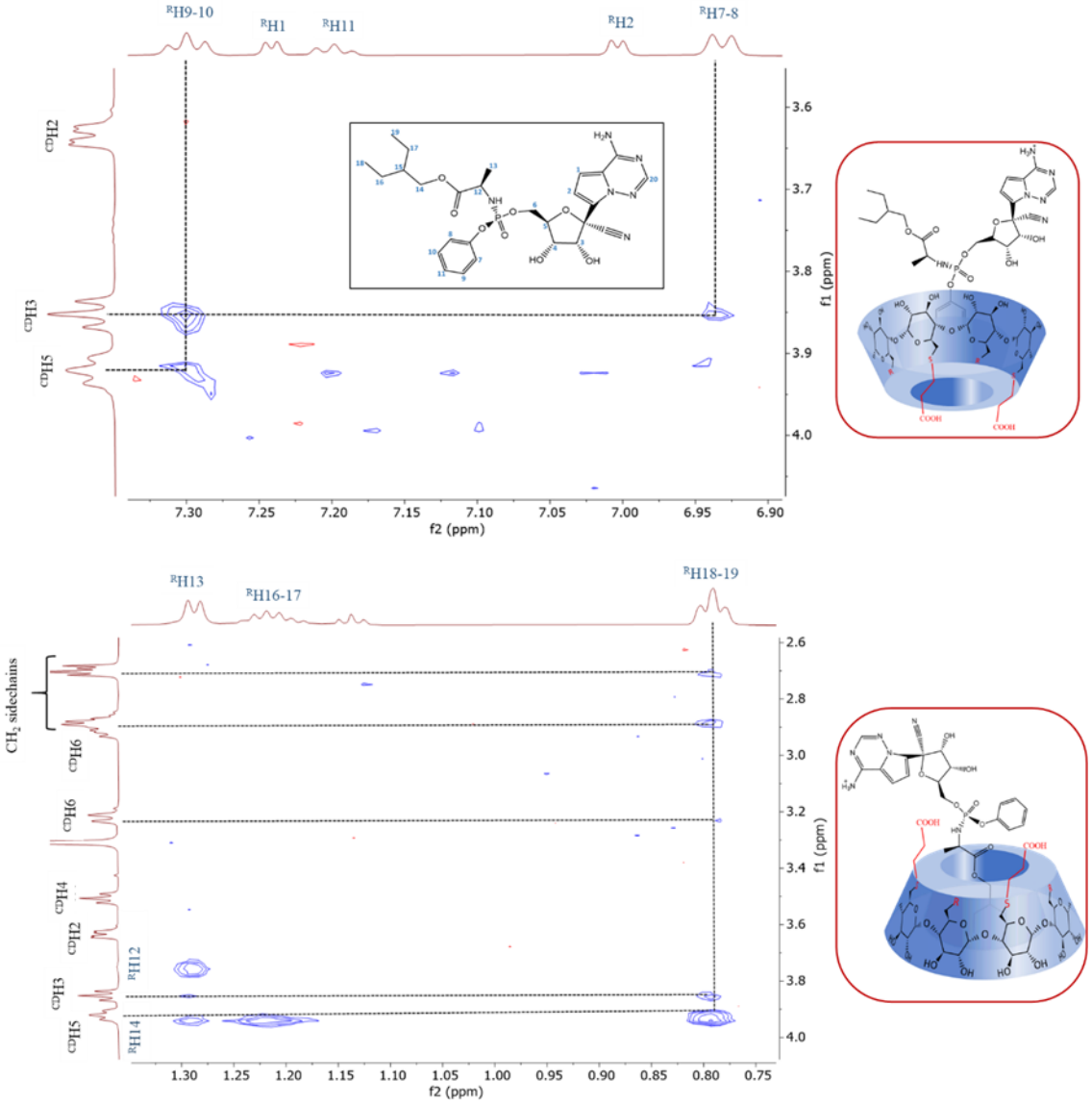

Figure 14. Partial 2D ROESY NMR spectra of the REM-sugammadex (1:2 molar ratio) sample and the suggested mode of REM insertion into sugammadex.

1.9. Mitragynine

1.9.1. Stoichiometry and stability constants of various MTR-CD complexes

The complex stoichiometry and stability constants of the two different MTR-CD systems (native MTR-βCD and MTR-SBEβCD) were determined by ^{1}H NMR titrations at pH 4.5. The complete ^{1}H and ^{13}C resonance assignments and registered spectra of uncomplexed MTR are given in the Table 3, respectively.

Table 3. Complete ^{1}H NMR resonance assignment for mitragynine in D_2O at pH 4.5, 600 MHz, ref. MeOH δ_H = 3.31 ppm).

No.	*^{1}H*
1	6.61 (d, J = 7.8 Hz, 1H)
2	7.11 (d, J = 7.8 Hz, 1H)
3	7.01 (d, J = 8.2 Hz, 1H)
4	-
5	-
6	-
7	-
8	-
9	3.16 (m, 1H)
9'	3.30 (m, 1H)
10	3.32 (m, 1H)
10'	3.66 (m, 1H)
11	4.11 (d, J = 7.8 Hz, 1H)
12	2.25 (m, 1H)
12'	2.59 (q, J = 10.9 Hz, 1H)
13	3.16 (m, 1H)
14	1.96 (m, 1H)
15	3.22 (m, 1H)
15'	3.59 (d, J = 13.0 Hz, 1H)
16 *16'*	1.40 (m, 2H)
17	0.80 (t, J = 7.4 Hz, 3H).
18	-
19	-
20	3.63 (s, 3H)
21	7.58 (s, 1H)
22	3.77 (s, 3H)
23	3.84 (s, 3H)

In order to determine the stoichiometry of complexation, an ^{1}H NMR titration was performed based on Job's method. Well-separated NMR signals of MTR were monitored in all experiments. In the case of the native βCD, Job's plot curves (Figure 15A) showed a maximum at x = 0.5. In contrast, several Job's profiles of MTR with SBEβCD exhibited maxima at different abscissa values (Figure 15B).

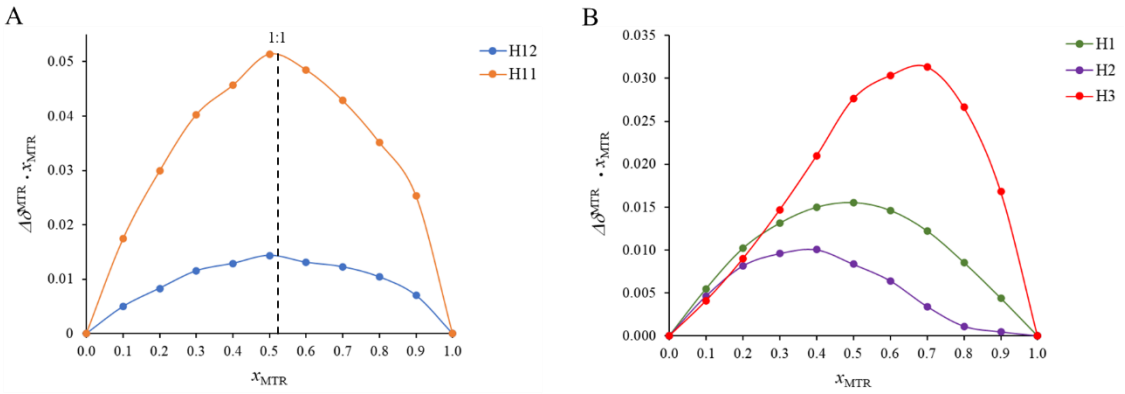

Figure 15. Job's plot for the selected ^{1}H resonances of MTR in the case of NMR titration with βCD (subplot A) and with SBEβCD (subplot B).

To determine the stability constants, separate ^{1}H NMR titrations were carried out. During the titration of MTR with βCD, the chemical shift changes of the following MTR ^{1}H resonances were monitored: H1, H2, H3, H11, H12, H12', H17 and H21, while in the case of the βCD, the H3 was followed. All the nine datasets were evaluated simultaneously with nonlinear regression using the OPIUM software (Figure 16). This global evaluation yielded a stability constant of log$K$ = 0.8 (0.2), given its estimated standard deviation in parenthesis.

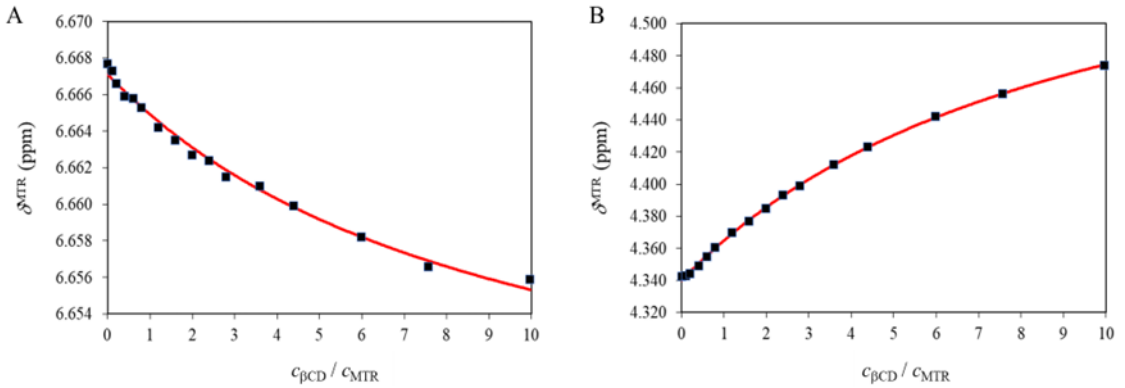

Figure 16. Chemical shift profile of the H1 (subplot A) and H10 (subplot B) resonances of MTR upon titration with βCD, fitted by the 1:1 complexation model using OPIUM program (red curves).

The behaviour of the selected MTR signals upon titration with SBEβCD is depicted in Figure 17A. To obtain reliable association constants, the chemical shifts of H1, H2, H3, H11, H12 and H17 MTR protons were selected to enter the multivariate evaluation. These datasets could not be fitted in a satisfactory manner by assuming either the formation of a single MTR·SBEβCD or a single 2MTR·SBEβCD complex. However, employing the two-species {MTR·SBEβCD, 2MTR·SBEβCD} model leads to perfect fitting of all the titration datasets, including the non-monotonic ones (see Figure 17B). This global fitting yielded an apparent stability constant of $\log\beta_{21}$ = 6.87 (0.10) for the 2MTR·SBEβCD and $\log\beta_{11}$ = 3.68 (0.03) for the MTR·SBEβCD complex.

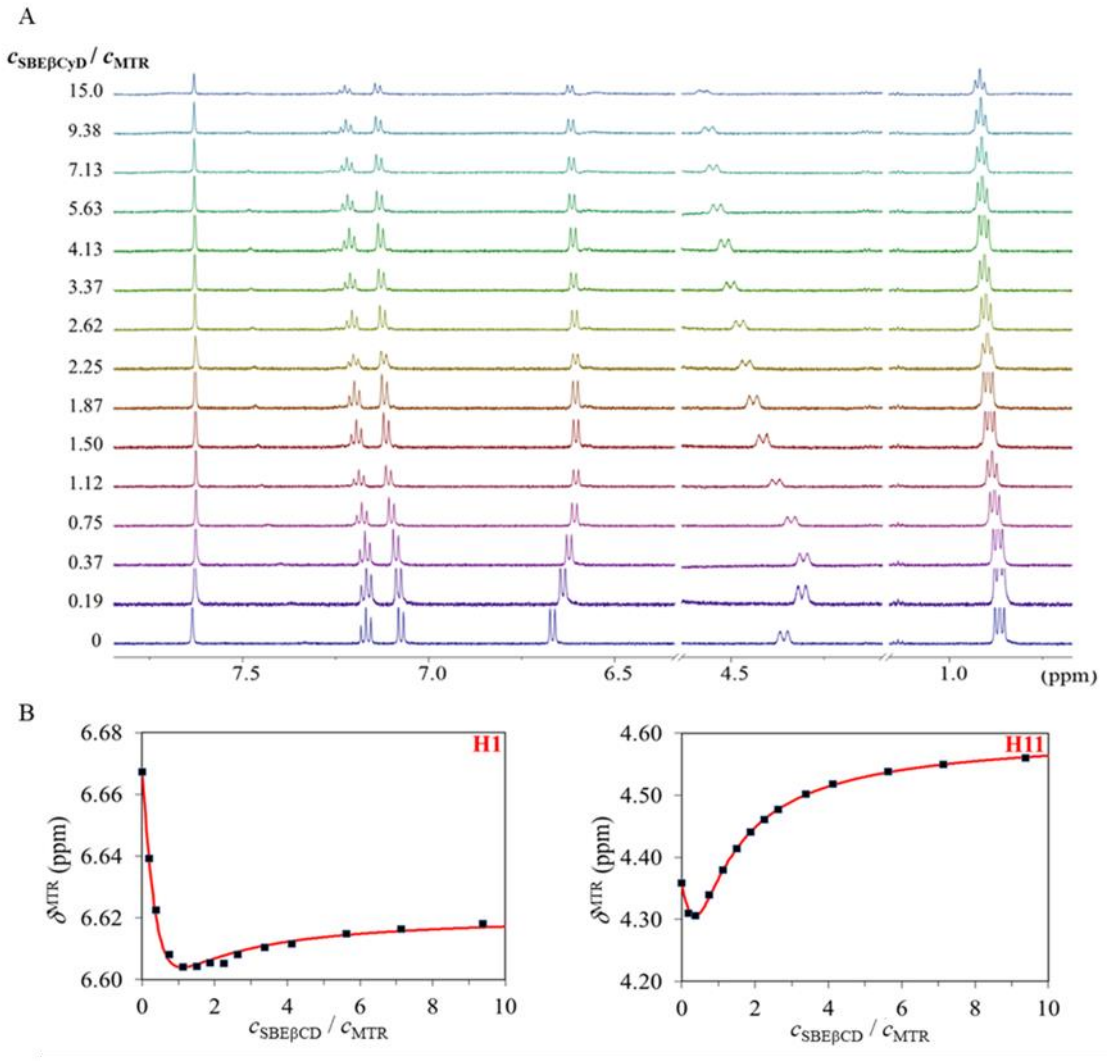

Figure 17. Representative ^{1}H NMR multiplet displacements (subplot A) of the MTR ^{1}H resonances upon titration with SBEβCD. Subplot B shows the selected titration profiles of the H1 and H11 MTR resonances. Red curves were fitted by assuming the presence of both the MTR·SBEβCD and the 2MTR·SBEβCD species.

1.9.2. Structural characterization of various MTR-CD complexes

To explore the possible structure of MTR-CD complexes, various 2D ROESY spectra were recorded. In the case of βCD, the host was applied in twofold excess in the NMR sample. Weak intermolecular NOE cross-peaks could be detected between the MTR's H1, H2, H3 protons and the inner cavity resonances of βCD (H3 and H5) (Figure 18A). Similar to βCD, cross-peaks were identified between the aromatic indole ring (H1, H2, H3) and the CD resonances for the MTR-SBEβCD sample with 1:2 molar ratio (Figure 18B). In this case it is difficult to evaluate the ROESY spectrum, because the randomly substituted SBEβCD (DS ~ 6.5) provides diffuse and broad NMR signals.

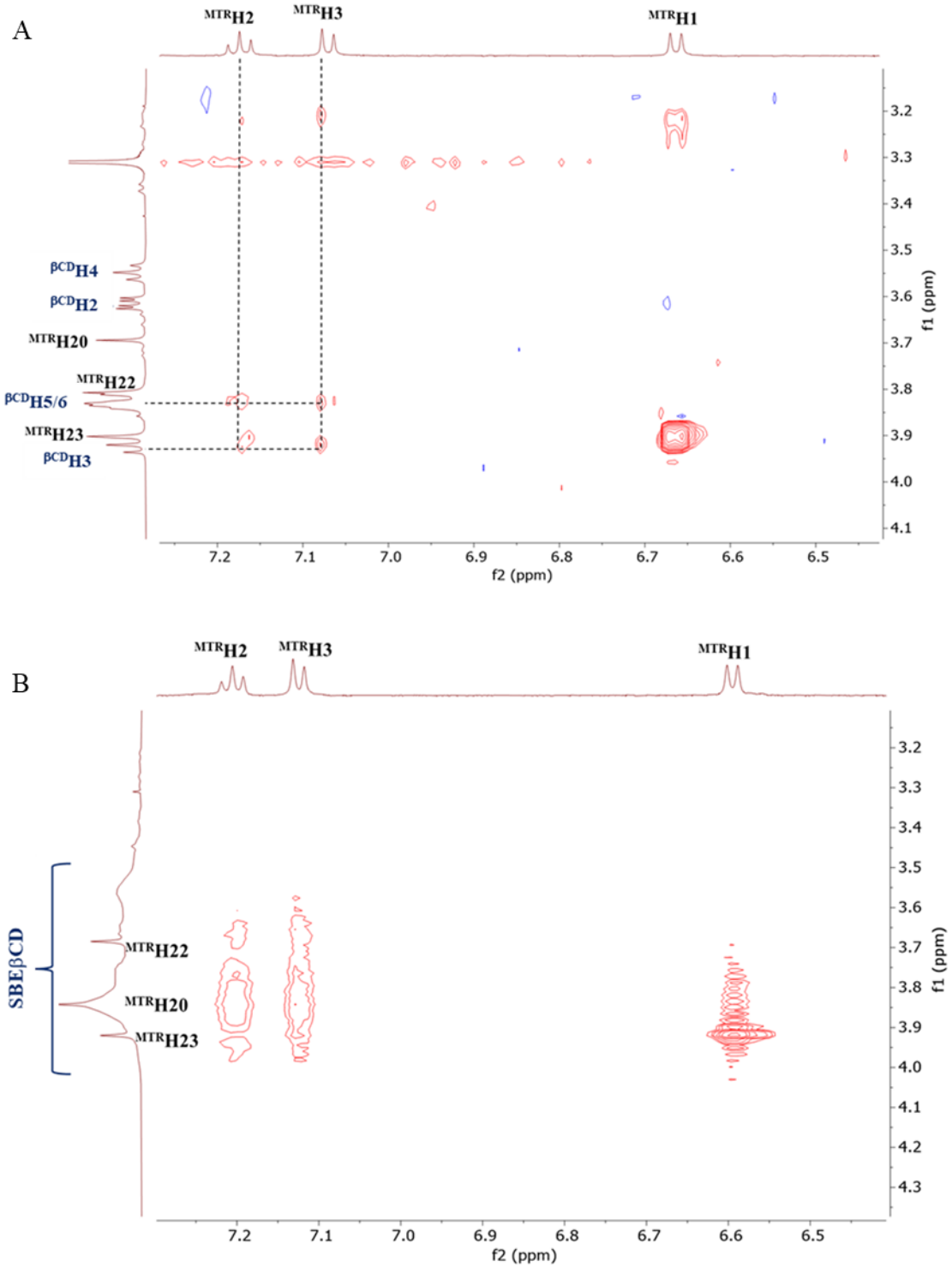

Figure 18. Partial 2D ROESY NMR spectra in the two studied MTR-CD complexes. Subplot A (1 MTR : 2 βCD molar ratio) showing cross-peaks between the aromatic MTR resonances and the inner cavity resonances (H5 and H3) of the βCD. Subplot B (1 MTR : 2 SBEβCD molar ratio) showing diffuse cross-peaks between the aromatic resonances of MTR and the SBEβCD protons.

1.10. Fondaparinux

1.10.1. Stoichiometry and stability constants of the FDPX-per-6-NH_2βCD complex

Intermolecular interactions between FDPX and per-6-NH_2βCD were investigated at two different pD values (pD 2.0 and 7.4), where the charge distribution of the interacting species is different. First, the complete ^{1}H NMR assignments of FDPX at pD 2.0 and pD 7.4 can be found in Table 4.

Table 4. ^{1}H NMR chemical shifts (in ppm) of fondaparinux (in D_2O at pD 2.0 and pD 7.4, ref. MeOH δ_H = 3.31 ppm).

Moiety	**GlcNS6S**		**GlcA**		**GlcNS3S6S**		**IdoA2S**		**GlcNS6S-OMe**	
Nucleus	***pD***		***pD***		***pD***		***pD***		***pD***	
	2.0	***7.4***	***2.0***	***7.4***	***2.0***	***7.4***	***2.0***	***7.4***	***2.0***	***7.4***
H1	5.50	5.58	4.61	4.58	5.42	5.47	5.20	5.14	4.97	4.98
H2	3.23	3.22	3.41	3.37	3.41	3.41	4.26	4.27	3.24	3.24
H3	3.54	3.58	3.81	3.80	4.34	4.33	4.22	4.12	3.65	3.61
H4	3.55	3.54	3.89	3.73	3.94	3.92	4.15	4.10	3.71	3.73
H5	3.71	3.85	4.06	3.91	3.90	4.12	5.08	4.71	3.93	3.91
H6	4.13	4.12			4.24	4.22			4.29	4.30
H6'	4.28	4.33			4.41	4.45			4.32	4.36
OMe									3.39	3.38

To assess the complex stoichiometry at pD 7.4, Job's plots were constructed from well-separated NMR resonances of FDPX, such as those of the anomeric protons of the GlcNS6S, GlcA and GlcNS3S6S residues, the H1 and H5 resonances of IdoA2S, and the anomeric H1 resonance of the per-6-NH_2βCD. All Job's plot curves depicted in Figure 19A show a maximum at x_{FDPX} = 0.5.

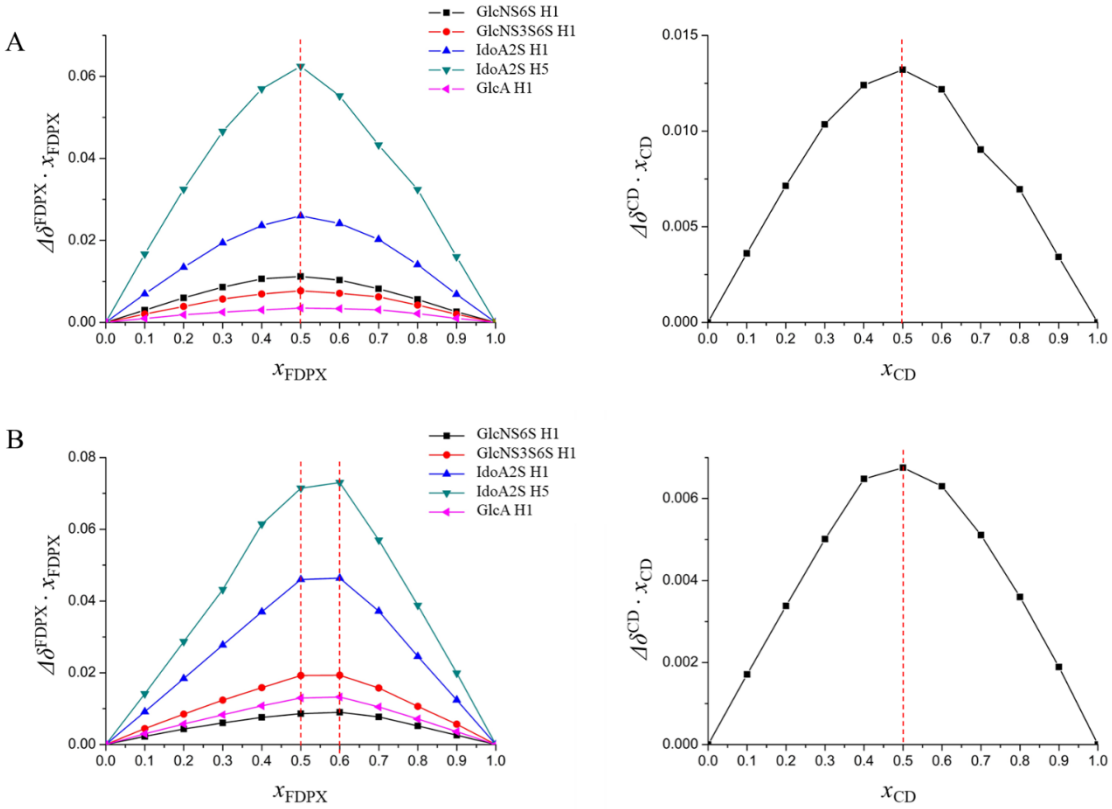

Figure 19. Job's plot for the selected ^{1}H resonances of FDPX at and the anomeric resonance of per-6-NH_2βCD at pD 7.4 (subplot A) and at pD 2.0 (subplot B), respectively. Herein the abbreviation of CD indicates per-6-NH_2βCD.

During the subsequent single-tube ^{1}H NMR titration of FDPX with per-6-NH_2βCD at pD 7.4 (see the stack plot in Figure 20A), the chemical shift variation of the following protons with non-overlapping resonances were monitored: GlcA H1, GlcNS3S6S H1, GlcNS6S-OMe H1, GlcNS3S6S H6, IdoA2S H5 and H1, GlcNS6S H1 of FDPX and H1 of per-6-NH_2βCD. Titration profiles of the latter two FDPX nuclei are depicted in Figure 20B. To extract a more robust and reliable, single value of this stability constant [23], the eight datasets were subjected to simultaneous nonlinear regression using the OPIUM software. The quality of fit remained virtually the same for all the observed nuclei and this global evaluation yielded $\log\beta_{11}$ = 3.65 with an estimated standard deviation of 0.02.

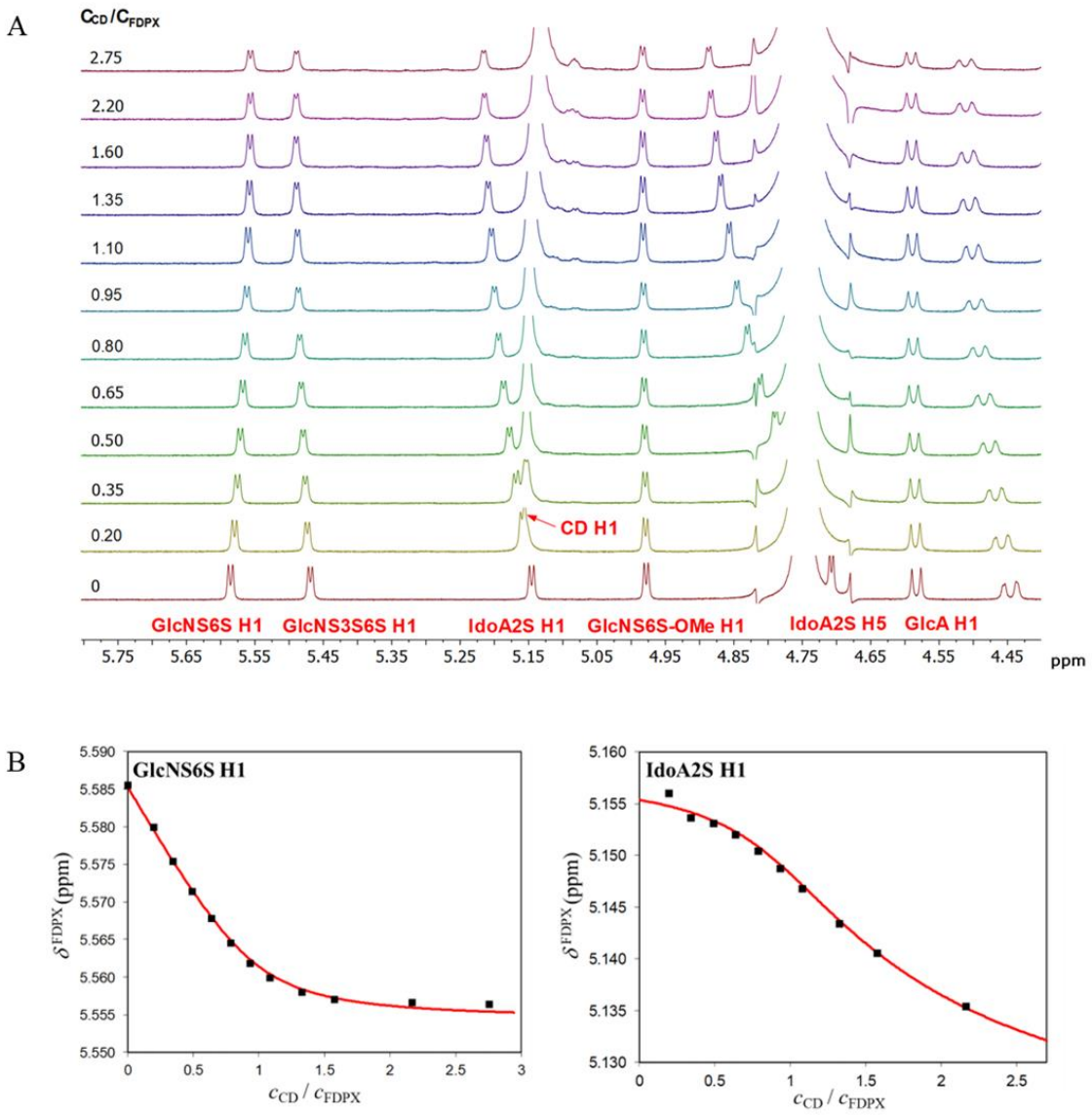

Figure 20. Representative ^{1}H NMR chemical shift changes (subplot A) of the FDPX ^{1}H resonances upon titration of 3.4 mM FDPX solution with increasing portions of a 20.1 mM per-6-NH_2βCD solution at pD 7.4. Titration profiles of FDPX GlcNS6S H1 and IdoA2S H1 (subplot B) at pD 7.4, fitted by the 1:1 complexation model using the OPIUM program (red curves). Herein the abbreviation of CD indicates per-6-NH_2βCD.

Job's plots recorded at pD 2.0 revealed a less clear-cut picture about complexation (see Figure 19, subplot B). The profile of the anomeric per-6-NH_2βCD proton is rather wide but bears a maximum at x_{CD} = 0.5, however depicted Job's plots of FDPX consequently shifted to ca. x_{FDPX} = 0.6.

To explore the complexation equilibria at pD 2.0 more thoroughly, a single-tube ^{1}H NMR titration of FDPX with the per-6-NH_2βCD was carried out. Titration profiles of the anomeric protons belonging to the GlcA, IdoA2S, GlcNS6SOMe, GlcNS6S,

GlcNS3S6S units and H5 of GlcNS3S6S as well as for the per-6-NH_2βCD anomeric proton (CD H1) are depicted in Figure 21. Hence the entire dataset cannot be fitted satisfyingly assuming the formation of a single FDPX·per-6-NH_2βCD complex, the titration curves were evaluated in two steps.

All experimental datasets can be nicely fitted up to $c_{CD}/c_{FDPX} = 1$ with the assumption of a single FDPX·per-6-NH_2βCD complex only (blue curves in Figure 21), yielding $\log\beta_{11} = 4.9 \pm 0.1$, but higher values of this stability constant give virtually the same goodness-of-fit. Addition of a 2FDPX·per-6-NH_2βCD species to the equilibrium model, as suggested by Job's plots, did not furnish a meaningful value for β_{21}, the iterations by the OPIUM program did not converge. Consequently, one cannot describe the monotonic change in FDPX chemical shifts beyond the equimolar composition by the {FDPX·per-6-NH_2βCD, 2FDPX·per-6-NH_2βCD} equilibrium model. Instead, an FDPX·2per-6-NH_2βCD complex was postulated besides FDPX·per-6-NH_2βCD. A global fitting involving these two species was now able to describe the titration profiles of FDPX and per-6-NH_2βCD protons in the full range of concentrations studied (see the fitted red curves in Figure 21). The calculations yielded a stability constant of $\log \beta_{12} = 8$ for the FDPX·2per-6-NH_2βCD complex (but this value again represents merely a lower limit).

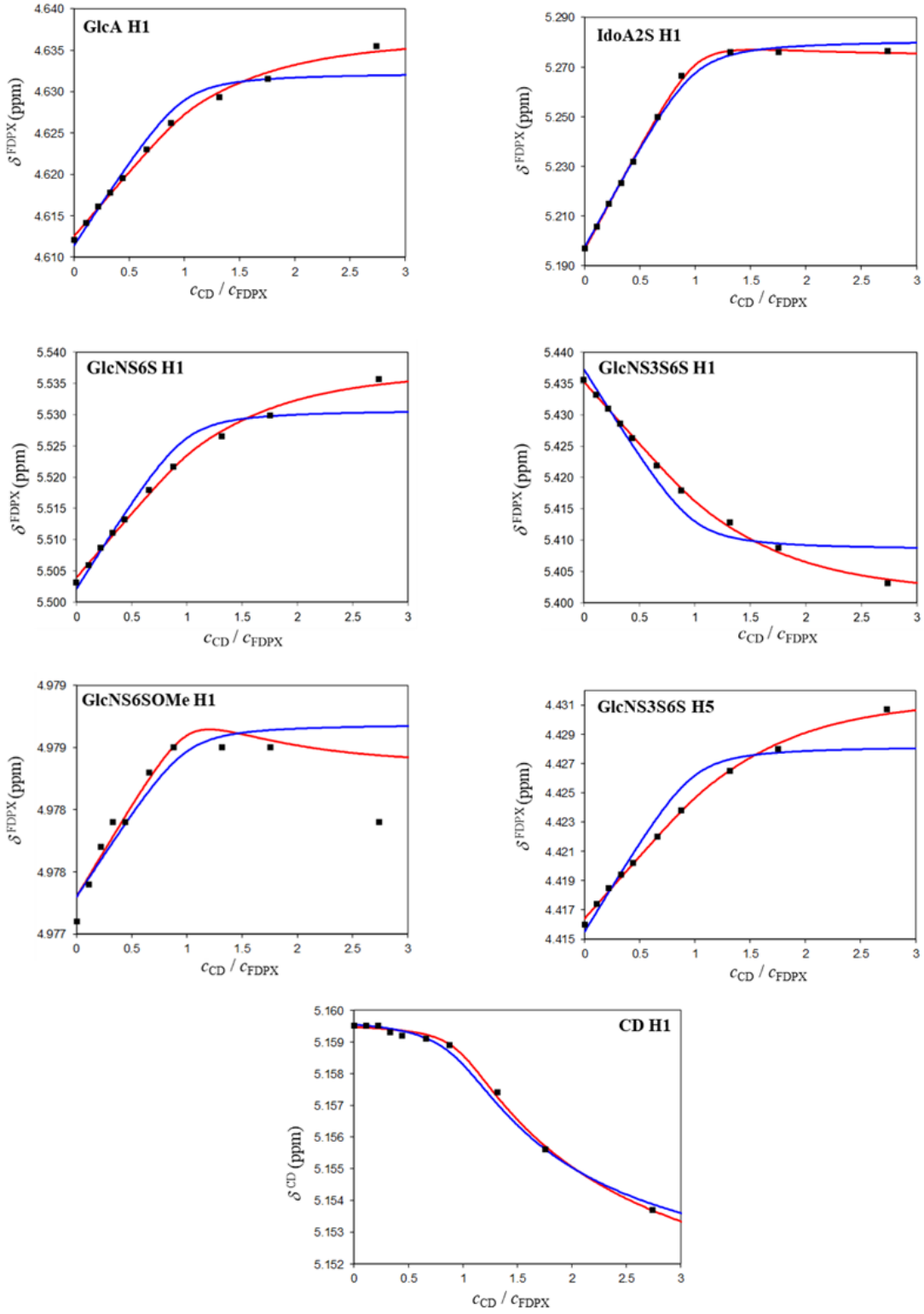

Figure 21. Titration profiles of the H5 nucleus of FDPX GlcNS3S6S and the anomeric protons of the FDPX GlcA, IdoA2S, GlcNS6SOMe, GlcNS6S, GlcNS3S6S and the per-6-NH_2βCD at pD 2.0. Blue curves were fitted by the 1:1 complexation model, while global fitting assuming the FDPX·per-6-NH_2βCD and the FDPX·2per-6-NH_2βCD species are shown by red curves. All titration curves were fitted by OPIUM program. Herein the abbreviation of CD indicates per-6-NH_2βCD.

1.10.2. Structural characterization of the FDPX-per-6-NH_2βCD complex

To obtain atomic-level information about the 3D structure of the FDPX-per-6-NH_2βCD complex, NOE experiments were carried out. Solutions at pD 2.0 - 7.4 were tested. The 2D NOESY spectrum for all pD values revealed that the H6 protons of the per-6-NH_2βCD give intermolecular contacts with the FDPX's IdoA2S H1 proton - as shown in Figure 22 for the pD 2.0 sample.

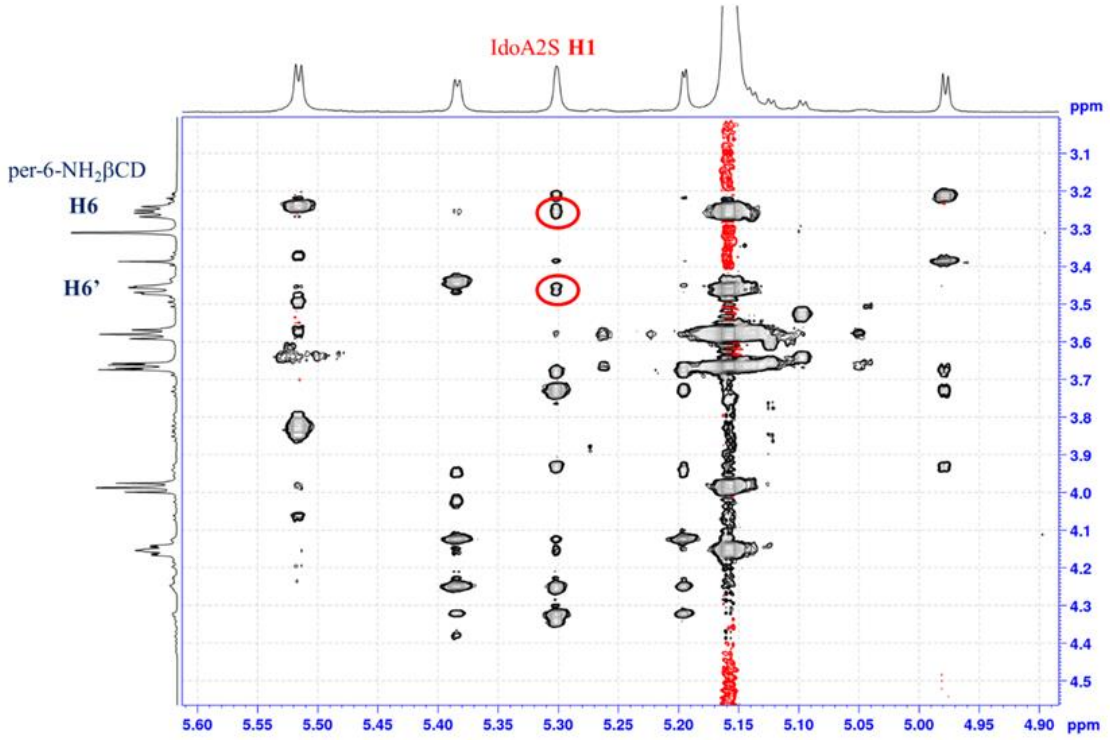

Figure 22. Partial 2D ROESY NMR spectra of a pD 2.0 sample containing FDPX and per-6-NH_2βCD at 1:1 molar ratio, showing cross-peaks between the IdoA2S H1 proton and the CD H6 resonance.

1.10.3. Characterization and stability analysis of the FDPX degradation product

Since no literature data were found regarding the degradation behaviour of FDPX, various experiments were performed. Recording the ^{1}H NMR spectra of aqueous FDPX sample at pD 2.0 after a week of storage indicated that new ^{1}H resonances appeared, see Figure 23.

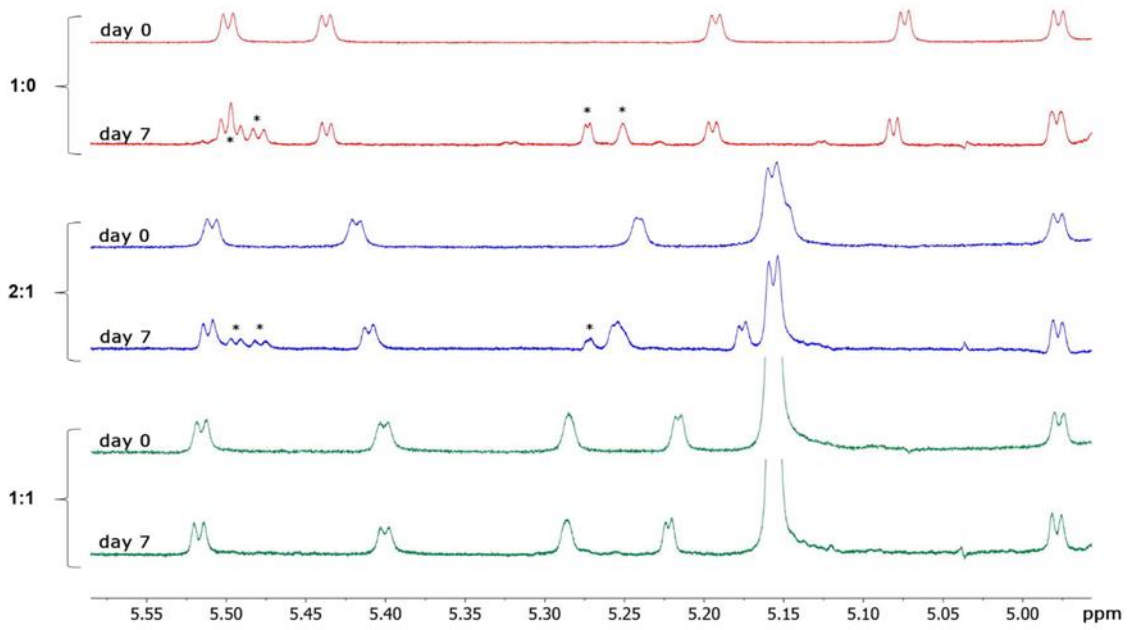

Figure 23. The ^{1}H NMR spectra of the freshly prepared FDPX-per-6-NH_2βCD samples (day 0) and that of the same samples stored at 25 °C for a week (day 7) at different molar ratios (red 1:0, blue 2:1, green 1:1) under pD 2.0 conditions. The ^{1}H resonances of the decomposition product are indicated by *.

In order to identify the structure of the degradation product, additional 2D NMR spectra were recorded. The spin system of the monosaccharide subunits of the degradation product was identified by COSY and TOCSY experiments, respectively. Furthermore, HSQC (Figure 24A) and 2D ROESY experiments (Figure 24B) was performed to prove the integrity of the pentasaccharide chain and to establish the connectivity of the monosaccharides.

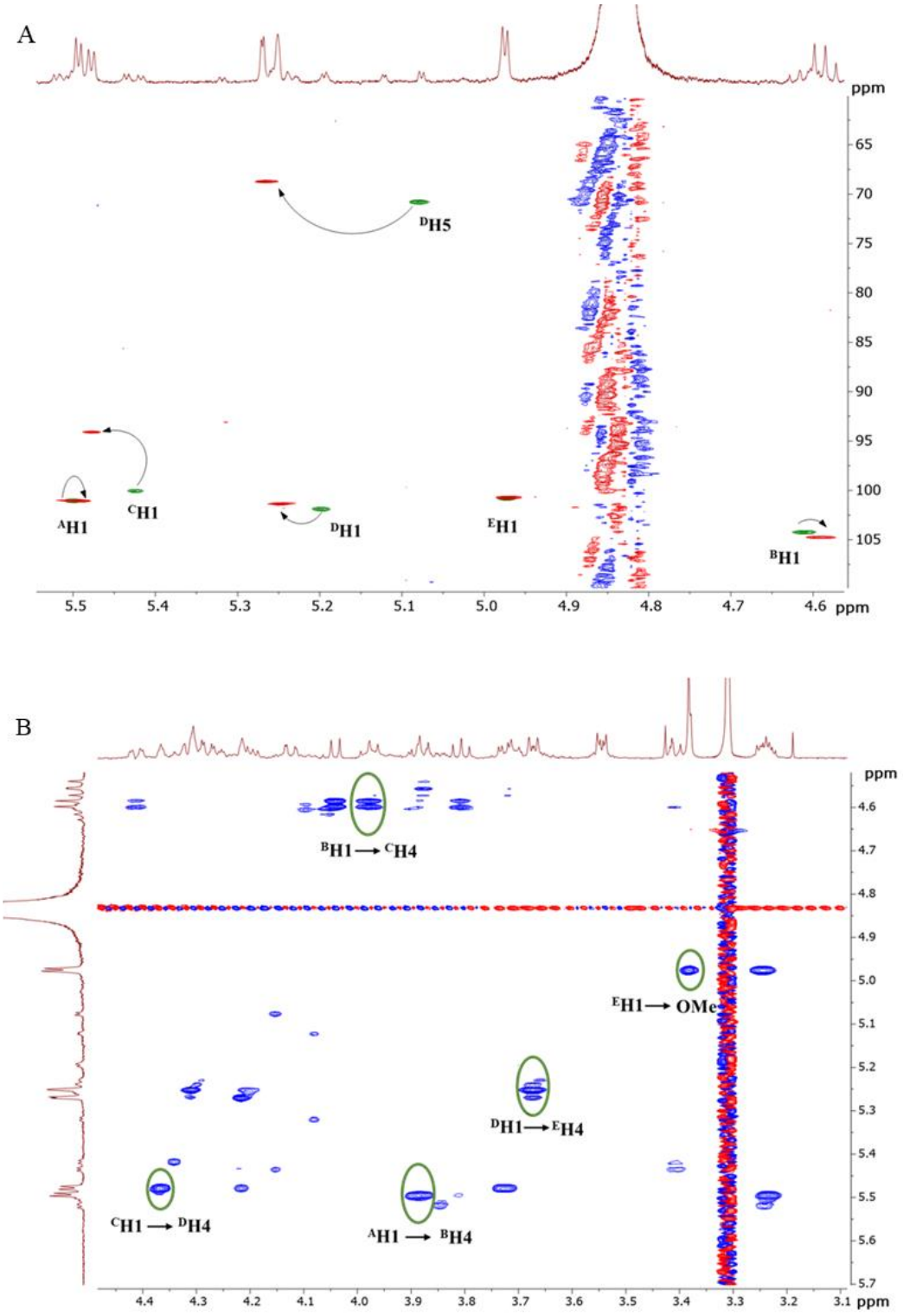

Figure 24. Subplot A shows the 2D HSQC NMR spectra comparison of the anomeric region of the freshly prepared (green) and the degraded (red) FDPX solutions at pD 2.0. Remarkable shift was detected in the case of the anomeric carbon of the GlcNS3S6S (subunit C) and the C5 resonance of the IdoA2S (subunit D) monosaccharide moiety. Partial 2D ROESY NMR spectra of the degraded FDPX at pD 2.0 is shown in sublot B. Highlighted cross-peaks providing evidence for the connectivity of monosaccharide subunits of the degraded FDPX.

To overcome the unwanted degradation of FDPX under acidic condition, the possible protective function of per-6-NH_2βCD was explored. To demonstrate the stabilizing effect of the per-6-NH_2βCD, ^{1}H NMR spectra of the freshly prepared pD 2.0 samples with 1:0, 2:1 and 1:1 (FDPX - per-6-NH_2βCD CD) molar ratios were recorded. All samples were incubated at 25 °C for a week, then ^{1}H NMR spectra were re-recorded (Figure 23).

To accelerate the decomposition of FDPX, samples with the same molar ratios were incubated at 60 °C for 14 hours. ^{1}H NMR spectra were registered prior and after the incubation at room temperature (Figure 25).

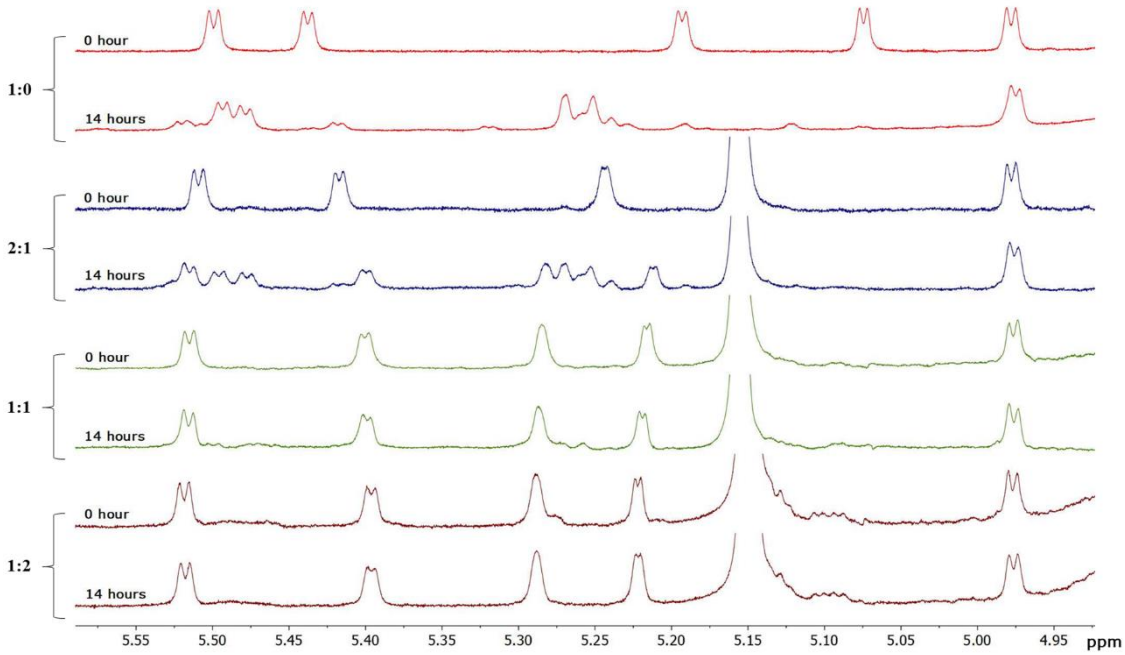

Figure 25. ^{1}H NMR spectra of various FDPX-per-6-NH_2βCD samples at molar ratios of 1:0 (red), 2:1 (blue), 1:1 (green) and 1:2 (brown) registered at 25 °C, prior (0. hour) and after (14 hours) incubation at 60 °C. FDPX degraded almost completely without per-6-NH_2βCD (red), while the process slowed down with increasing per-6-NH_2βCD concentration.

DISCUSSION

1.11. Remdesivir

1.11.1. Determination of the pK_a value of REM by UV-pH titration method

So far there was no experimentally supported literature data on the pK_a value of REM, only predicted (in silico) data are available [65]. In our case it is important to have an accurate value regarding pK_a since protonation state influences the intermolecular interactions between REM and CDs. Acidifying the solution results in hypochromic and hypsochromic effects in the range of 240-250 nm, while hyperchromic and bathochromic effects could be observed in the range of 280-320 nm (see Figure 6). The largest changes in the absorbance values were observed at ~245 and ~303 nm. Based on the simultaneous fitting of all titration datasets for all wavelengths the resulting pK_a value (3.56) indicates that at least 97% of REM molecules are present in monoprotonated form under pH 2.0 conditions – where all our experiments were exported.

1.11.2. Stoichiometry and stability constants of various REM-CD complexes

Based on Job's experiment results, all six investigated supramolecular systems have a maximum at 0.5, suggesting 1:1 complex stoichiometry. Afterward all titration curves were fitted regarding 1:1 stoichiometry with Origin. Comparing the determined log$K$ values, shown in Table 2 in case of the native CDs, a tenfold decrease in stability could be observed when using γCD. Generally, the introduction of the anionic sulfobutylether-sidechains on the CD hosts contribute to a significant stability enhancement (more than fivefold for γCD, while tenfold increase for βCD, respectively), resulting in a high affinity system for REM and SBEβCD (averaged and apparent log$K$ = 3.99) [66]. It has also been revealed that the number of the anionic sidechains located on the primary side of the host plays a critical role in the stability of the inclusion complex. The single isomer sulfobutylether-CD (per-6-SBEβCD) results in an additional two-fold increase in stability with the monoprotonated REM compared to the random SBEβCD, owing to the seven anionic sidechains located on the same rim (primary side) of the host. Based on the data of our research group, sugammadex is almost fully protonated under pH 2.0 conditions [67], besides possesses shorter sidechains than the sulfobutylether-CD

derivatives, therefore limited electrostatic interactions can occur between the host and REM. The obtained stability constant indicates much weaker intermolecular interactions compared to the permanently negatively charged CDs.

1.11.3. Structural characterization of various REM-CD complexes

To gain deeper insight into the structure of the different CD-REM complexes 2D ROESY NMR spectra were recoded.

A zoomed inset in Figure 9 refers spatial proximities between the ethylbutyl-sidechain of REM and the inner cavity of βCD, proving that the aliphatic moiety is immersed into the host cavity. The encapsulation of alkyl chains is well-known in the literature, especially in the case of lipids [68]. As REM also possesses a rather lipophilic phenoxy moiety, its inclusion was also anticipated, however no inclusion of the phenoxy moiety was observed in this case. There are examples even in our research where the immersion of branched alkyl sidechains is preferred in the presence of an aromatic moiety [69]. The inclusion of the ethylbutyl-sidechain was also corroborated by a further interaction between the methyl resonance of the alanyl residue (H13) and the H6 methylene of the βCD, which unequivocally confirms that the inclusion occurs from the narrower rim of the CD (see Figure 9).

In case of the single isomer per-6-SBEβCD the observed cross-peaks between the alanyl residue (H13) and the H6 resonance of the CD determined the penetration of the ethylbutyl-moiety of REM into the CD's cavity from the narrower rim (Figure 10). Thus, the proposed arrangement allows the formation of electrostatic interactions between the CD's negatively charged sulfobutyl-sidechains and the REM's protonated heterocyclic moiety, thereby supporting the observed increase in complex stability.

The structure of the SBEβCD-REM complex is difficult to determine, due to the random substituted nature of SBEβCD, i.e. it carries sulfobutyl-sidechains at position 2, 3 and 6 as well. Observed cross-peaks between the two molecules suggested that the aliphatic moiety was immersed into the cavity of the cyclodextrin. Cross-peak between the alanyl residue (H13) and the CD's sidechains confirms that the inclusion geometry can be further supported by an ionic interaction between the anionic host and the cationic guest (Figure 11).Taking into consideration the identical inclusion mode for both βCD and per-6-SBEβCD along with the stability values, it has been proposed that the SBEβCD-REM complex is also constructed in the same fashion (see Figure 11).

In the case of γCD only weak cross-peaks were observed on the registered ROESY spectrum (Figure 12). However, clear evidence indicates that the phenoxy ring immerses into the cavity of γCD from its narrower side, supporting a weak interaction between γCD and REM. While the sulfobutylation of γCD resulted in stability enhancement, no conclusive complex structure could be derived due to broadened and diffuse NMR signals (Figure 13).

The single isomer γCD derivative sugammadex allowed a detailed NMR characterization of REM complexation. Co-existence of at least two different complexes could be deducted based on the orientation of REM into sugammadex's cavity (Figure 14). The most pronounced interaction was the immersion of the phenoxy moiety into the cavity from the wider rim. Moreover, the methylene units of the thiopropionic groups of sugammadex show spatial proximity with the aliphatic chain of REM (H18-19), however this interaction lacks real inclusion of REM into the cavity. The intermolecular interaction is therefore established through the peripheral (thiopropionic acid) groups of sugammadex and the alkyl sidechain of REM. Thus, REM complexation with sugammadex accommodates several geometries leading to a superior stability.

1.12. Mitragynine

1.12.1. Stoichiometry and stability constants of various MTR-CD complexes

To determine the stoichiometry of the two supramolecular systems (MTR-βCD and MTR-SBEβCD), Job's method was employed. In the case of βCD the common scenario was observed as the curve maximum at 0.5 unequivocally indicated a 1:1 complex stoichiometry (MTR·βCD).

However, the different maxima observed on Job's plots for SBEβCD (Figure 15B), suggested that at least two complex species are present simultaneously in the supramolecular system. Furthermore, during circular dichroism (CiD) experiments the Hill coefficient (> 1) also suggested the prevalence of complexes exceeding the simple 1:1 stoichiometry [70].

In a new series of MTR titrations with βCD, chemical shift changes in eight MTR and one βCD ^{1}H signals were registered. Subsequently, the titration curves for all nine datasets were simultaneously fitted. The obtained stability constant of the MTR·βCD complex (log$K$ =0.8) indicates a remarkably weak interaction. This low binding affinity

between MTR and the βCD is also supported by the fact that even with a tenfold excess of the host used during titration, the inflection point of the titration curve remained unattainable (as depicted in Figure 16), resulting in a complexation degree of only 2.8%. A more precise determination of the formation constant would have required the recording of higher sections of the binding isotherm [22], but titration with a more concentrated stock solution was hindered by the limited aqueous solubility of βCD.

The titration of MTR with SBEβCD resulted in the non-monotonic displacement of certain multiplets (Figure 17), suggesting the coexistence of at least two complex species, in accordance with the interpretation of the Job's plots. In this case six different MTR resonances were monitored during the titration. A proper fitting of the titration curves was managed by assuming a complex supramolecular system including of two-species {MTR·SBEβCD, 2MTR·SBEβCD} at the same time. It is unique, however not unprecedented [71,72] that βCDs associate with two guest molecules, producing a mixture of 2:1 and 1:1 complexes. The intrinsic chemical shift values of the species are collected in Table 5 and the speciation curves in Figure 26 were constructed for the concentration range explored in the NMR titration.

Table 5. ^{1}H NMR chemical shifts (in ppm) of the uncomplexed and complexes species along with the stability constants of the 1:1 and 2:1 complexes (MTR titration with SBEβCD) computed by simultaneous fitting of all titration profiles with the OPIUM program (uncertainties in parenthesis are estimated standard deviations for the last significant digit).

Nucleus	δ_{MTR}	$\delta_{MTR\cdot SBE\beta CD}$	$\delta_{2MTR\cdot SBE\beta CD}$
H1	6.6678 (12)	6.6203 (8)	6.5319 (103)
H2	7.1695 (12)	7.2312 (9)	7.1325 (56)
H3	7.0744 (12)	7.1423 (8)	7.0795 (35)
H11	4.3549 (13)	4.6067 (17)	4.0321 (328)
H12	2.3595 (12)	2.4563 (9)	2.3005 (80)
H17	0.8663 (12)	0.9225 (8)	0.8432 (46)

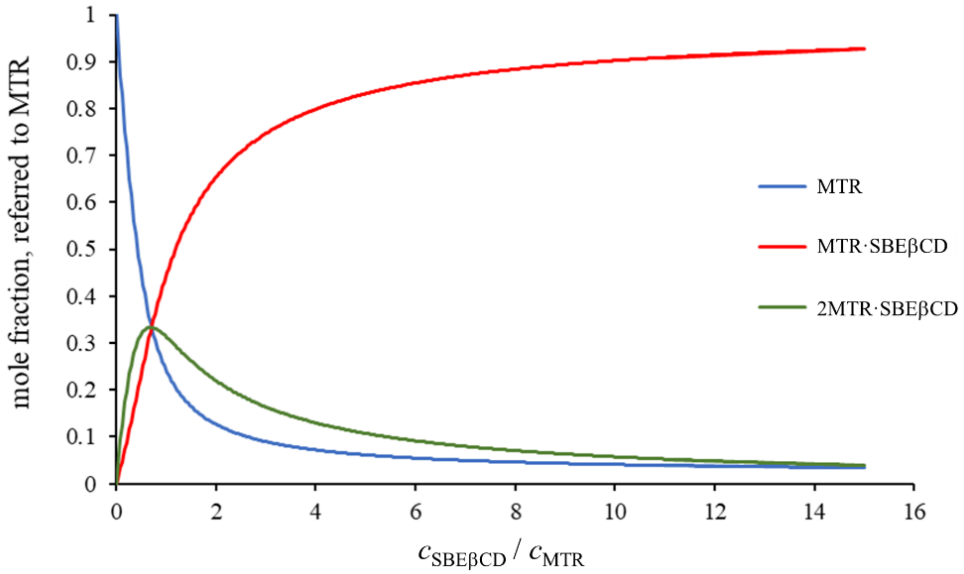

Figure 26. Species distribution plots for the ^{1}H NMR titration of MTR with SBEβCD.

Comparing to the native βCD (log$K$ = 0.8), this outstandingly large increase (logβ_{21} = 6.87 and logβ_{11} = 3.68) in complex stability could be supported by the possibility of electrostatic interactions between the fully ionized sulfonate groups on the host and the (at pH 4.5) fully protonated cationic guest molecule (MTR has a pK_a value of 8.1 [73]). The sulfobutylation also provides an enlarged cavity due to the butyl sidechains situated at both the primary and secondary rim of the host, thereby enhancing the encapsulation of the tetracyclic MTR. The flexibility of the sidechains can also contribute to an electrostatically anchored complexation leading to a much tighter insertion.

The result of supplementary CiD spectroscopic titration experiments was also in a good agreement with the logβ_{11} stability constant of the {MTR·SBEβCD, 2MTR·SBEβCD} system determined earlier by ^{1}H NMR titration [70].

1.12.2. Structural characterization of various MTR-CD complexes

Based on the registered 2D ROESY spectrum of MTR - βCD, intermolecular cross-peaks indicate not only the inclusion of the aromatic moiety into the βCD cavity (Figure 18A), but also direction of the immersion of MTR, which occurs from the wider rim of the βCD.

Cross-peaks in the ROESY spectrum of MTR - SBEβCD also indicates the immersion of the aromatic indole moiety into the CD cavity. The proposed structure of the 1:1 inclusion complex in the MTR·SBEβCD system is shown in Figure 27. The inclusion of

the indole moiety into the apolar cavity of the host was further confirmed during CiD experiments [70]. However, in this case it is difficult to determine the exact structure of the complex at atomic level, owing to the random distribution of sulfobutyl sidechains at positions O2, O3 and O6 of each glucose unit. Thus, the formation of a 2MTR·SBEβCD complex could be possible due to the negatively charged sidechains both on the narrower and the wider rim of the βCD- electrostatic interactions may occur. During the complexation, the greatest chemical shift displacement values could be observed in the case of the H10 MTR resonance ($\Delta\delta$ > 100 ppb), suggesting that the protonated tertiary amine should be involved in the complexation through electrostatic interaction.

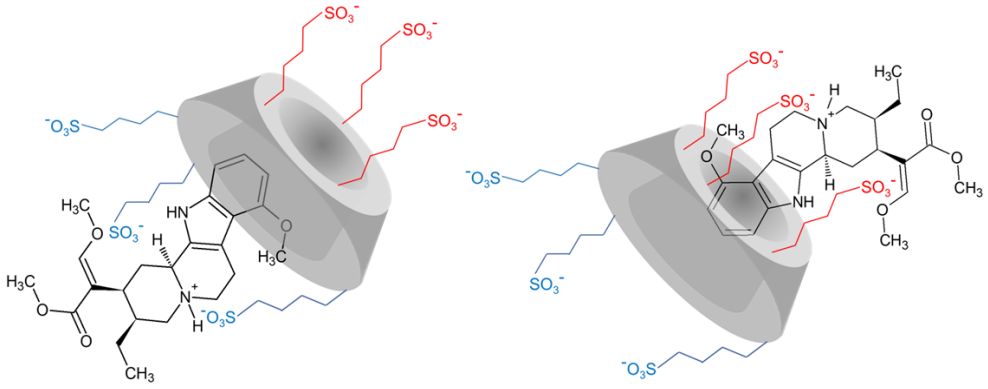

Figure 27. Suggested structure of the MTR·SBEβCD inclusion complex based on the registered 2D ROESY NMR spectra.

1.13. Fondaparinux

1.13.1. Stoichiometry and stability constants of the FDPX-per-6-NH$_2$βCD complex

At physiological pD value, the per-6-NH$_2$βCD bears an average positive charge of 5.1 (pK_a values for the per-6-NH$_2$βCD are as follows: 9.50(1), 8.89(1), 8.33(1), 8.07(1), 7.57(1), 7.35(1), 6.75(1) [74]), while at pD 2.0 the host is fully protonated, carrying seven positive charges. While in FDPX at pD 7.4 both hexuronic acid residues are deprotonated, therefore FDPX possesses 10 negative charges based on the published pK_a values of related oligosaccharides (pK_a of 2.35 for β-D-GlcA and a pK_a of 3.44 for IdoA2S) [75]. Under acidic conditions (at pD 2.0), the average charge of FDPX corresponds to -8.3.

After all the Job plots at pD 7.4 suggested the sole formation of the FDPX·per-6-NH_2βCD complex with 1:1 stoichiometry, titration curves were also fitted assuming the single FDPX·per-6-NH_2βCD complex. The determined stability constant (log*K* 3.56) indicates a moderately strong binding affinity for a single FDPX·per-6-NH_2βCD complex.

Under pD 2.0 conditions the Job's plot (Figure 19B) of the per-6-NH_2βCD ^{1}H NMR resonances suggested again a simple 1:1 complexation stoichiometry, however the extrema of the depicted FDPX proton curves are shifted to x_{FDPX} = 0.6, indicating the presence of a 2 FDPX : 1 per-6-NH_2βCD complex besides the 1:1 stoichiometry.

Most titration profiles of FDPX protons consist of two quasi-linear segments, with a minimal curvature near the crossing point at $c_{CD} = c_{FDPX}$ (see Figure 21) This type of titration curve is characteristic of a rather high-affinity system, for which merely the lower limit of the binding constant is accessible by curve-fitting [22]. The entire dataset cannot be fitted satisfyingly assuming the formation of a single 1 FDPX : 1 per-6-NH_2βCD complex (see the blue curves in Figure 21), the Hamilton's R factor, a goodness-of-fit criterion for the simultaneous fitting of the seven datasets, is 0.031%. However, using a global fitting that involved 1 FDPX : 2per-6-NH_2βCD complex besides 1:1, the Hamilton's R factor decreased to 0.0089%, indicating a more appropriate equilibrium model. See fitted titration curves in Figure 21 (red curves). The intrinsic chemical shift values of species are collected in Table 6. Using these lower limits of the stability constants, the speciation curves in Figure 28 were constructed for the concentration range explored in the NMR titration.

Table 6. ^{1}H NMR chemical shifts of uncomplexed and complexed species (in ppm units) along with the stability constant of the 1:1 and 1:2 complexes at pD 2.0, computed by simultaneous fitting of all titration profiles with the OPIUM program. Uncertainties in parenthesis are estimated standard deviations referring to the significant digit. Herein the abbreviation of CD indicates per-6-NH_2βCD.

Nucleus		δ_{FDPX} or δ_{CD}	$\delta_{FDPX\cdot CD}$	$\delta_{FDPX\cdot 2CD}$
FDPX	GlcNS6S H1	5.5039 (3)	5.5246 (5)	5.5388 (7)
	GlcA H1	4.6125 (3)	4.6282 (5)	4.6374 (7)
	GlcNS3S6S H1	5.4353 (3)	5.4153 (5)	4.6374 (7)
	IdoA2S H1	5.1966 (3)	5.2805 (5)	5.2739 (7)
	GlcNS6SOMe H1	4.9773 (3)	4.9788 (5)	4.9783 (7)
	GlcNS3S6S H5	4.4164 (3)	4.4250 (5)	4.4325 (7)
per-6-NH_2βCD H1		5.149 (3)	5.1595 (2)	5.156 (2)

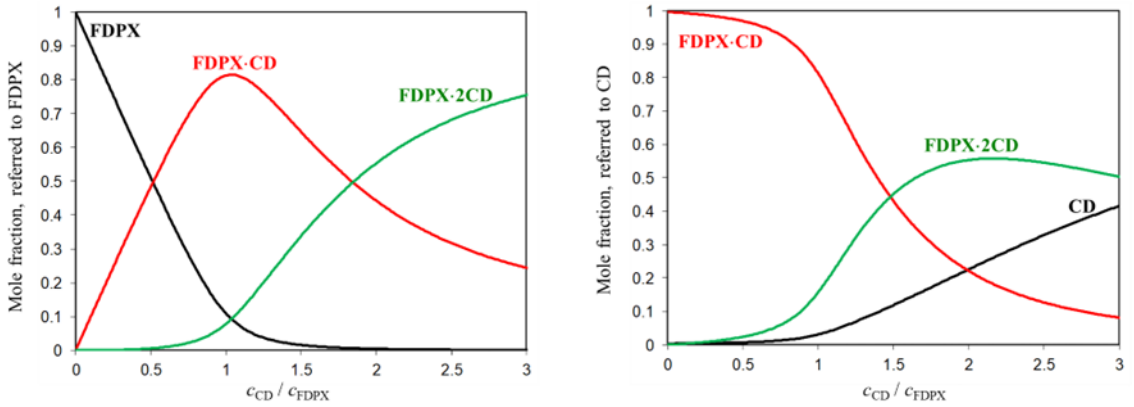

Figure 28. Species distribution plots for the ^{1}H NMR titration at pD 2.0. Herein the abbreviation of CD indicates per-6-NH_2βCD.

The discrepancy of Job's method and the chemical shift titration in establishing the correct stoichiometry of complexation is somewhat puzzling. Nevertheless, recent publications [76,77] emphasize the limitations of Job's method of equilibrium systems beyond the simplest 1:1 case, being highly sensitive e.g., to the ratio of equilibrium constants [76]. While Job's method remains a reliable tool in stoichiometric studies of inorganic metal complexes, a careful inspection of the distribution of residuals of data-fitting [23,76] or the ranking of all reasonable binding models based on estimated uncertainties and other chemometric descriptors [77] became the recommended protocols for the same task in the field of supramolecular chemistry. Since the

{FDPX·per-6-NH_2βCD, FDPX·2per-6-NH_2βCD} equilibrium model nicely reproduced the entire titration dataset, the formation of these two species can be regarded as most probable under the applied experimental conditions for this high-affinity system.

1.13.2. Structural characterization of the FDPX-per-6-NH_2βCD complex

Samples without phosphate buffer were used to investigate the structure of the complexes under pD 2.0 and 7.4 conditions, to eliminate any possible interfering effect of the phosphate ions with the per-6-NH_2βCD. NOE experiments were performed at several FDPX - per-6-NH_2βCD molar ratios, however, none of the experiments confirmed dipolar correlations between the inner protons of the per-6-NH_2βCD and FDPX (see Figure 22). Hence only outer-sphere, electrostatics-driven interaction can occur between these oligosaccharides (cross-peaks were identified between the per-6-NH_2βCD and the IdaA2S moiety of FDPX).

1.13.3. Characterization and stability analysis of the FDPX degradation product

It is well known from the literature, that sulfated polysaccharides can undergo degradation (depolymerization and/or desulfation) under acidic conditions. However, there were no detailed studies that provide relevant information on FDPX. Thus, samples under acidic conditions (pD 2.0) were investigated.

To determine the structure of the degradation product various NMR measurements were carried out. Registered 2D ROESY spectrum (Figure 24B) evidenced that the pentasaccharide chain remained intact during the applied circumstances of degradation. Therefore, the observed chemical shift changes upon decomposition cannot be attributed to the depolymerization of the FDPX backbone. Consequently, as supported by earlier studies on the acid hydrolysis of sulfated polysaccharides [78], sulfate loss of FDPX occurred in our case. Seto *et al.* followed the chemical shift changes in heparin undergoing desulfation by ^{1}H NMR measurements [79]. Their result also supports our data, as desulfation leads to downfield shift of resonances. After the full ^{1}H NMR assignment of the degradation product the largest chemical shifts changes ($\Delta\delta$) were observed in the case of the IdoA2S and the trisulfated (GlcNS3S6S) subunits (Figure 29), in agreement with the ^{13}C shift changes based on the HSQC spectrum (Figure 24A). These are suggesting that the sulfate loss primarily affected the IdoA2S and the GlcNS3S6S units. According to Kozlowski et al., the initial desulfation preferences of

heparin in acidic environments can be approximated by: 6OS < 2OS ≪ NS [80,81]. As the major change in ^{1}H chemical shifts (320 ppb) can be observed at H2 of GlcNS3S6S it indicates that structural change is occurring at that site of the C ring. Thus, we concluded that the sulfate loss in our case appears on the trisulfated GlcNS3S6S subunit, in the form of *N*-desulfation.

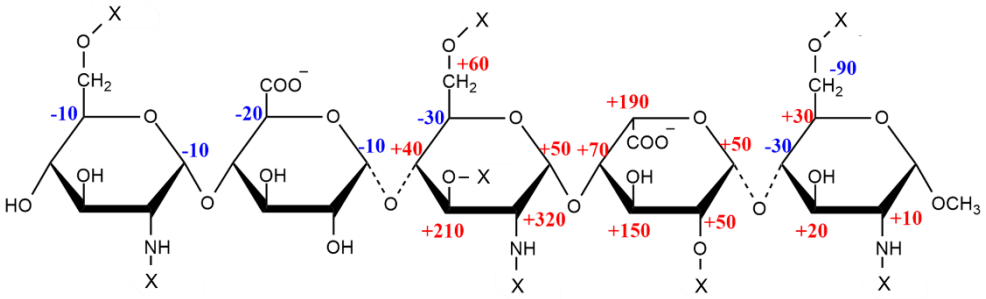

Figure 29. ^{1}H NMR chemical shift differences (in ppb) between the degradation product and FDPX. Significant $\Delta\delta$ values were observed for the ^{1}H resonances of the inner GlcN and the adjacent IdoA moieties suggesting the site(s) of desulfation(s). (X = SO_3^- or H).

During the demonstration of the stabilizing effect of the per-6-NH_2βCD shown in Figure 23, almost 50% of the FDPX degraded in the absence of per-6-NH_2βCD in a week. The decomposition process slowed down significantly in the presence of half equivalent per-6-NH_2βCD, as only 20% degradation could be observed by ^{1}H NMR. However, samples of equimolar FDPX and per-6-NH_2βCD revealed no detectable degradation of FDPX. Applying even higher molar ratios of per-6-NH_2βCD, complete protection of FDPX was observed, therefore a minimum of equimolar per-6-NH_2βCD is necessary to prevent desulfation.

Throughout accelerated degradation studies at 60 °C (shown in Figure 25) sample without per-6-NH_2βCD degraded completely, while those containing per-6-NH_2βCD exhibited less pronounced desulfation. In the presence of 1:1 molar ratio minor degradation could be observed, while molar excess of per-6-NH_2βCD (1:2 molar ratio) completely hindered the desulfation.

Furthermore, additional mass spectrometry (MS) experiments supported the NMR spectroscopic findings, utilizing the beneficial stabilizing effect of the per-6-NH_2βCD of FDPX in the gas phase. MS data provided evidence that the degradation products of FDPX are pentasaccharides with an intact glycan backbone, displaying predominantly one, and to a lesser extent two sulfate losses [82].

CONCLUSIONS

In the case of REM, NMR spectroscopic studies revealed that introduction of the anionic sulfobutylether-sidechains on the CD hosts significant enhances the complex stability. Additionally, the primary side sulfobutylation of the host plays key role in the stability of the inclusion complex. Based on 2D ROESY NMR experiments it has been revealed that mainly the ethylbutyl moiety is involved in the molecular encapsulation in REM-βCD systems. Moreover, the inclusion of the phenoxy moiety was only observed in the case of γCD derivatives. In addition, the pK_a value of REM (pK_a = 3.56) was determined experimentally by UV-pH titration method here for the first time.

^{1}H NMR titration studies revealed a rather weak interaction (logβ_{11} = 0.8; MTR·βCD) between MTR and βCD, whereas a significantly stronger was observed in the case of SBEβCD (logβ_{11} = 3.68, logβ_{21} = 6.87) and the co-existence of both 1:1 and 2:1 MTR-SBEβCD complexes was deduced. Sulfobutylation of βCD yielded a 750-fold increase in the apparent stability of the supramolecular system due to the enlarged cavity, sidechain flexibility and the possibility of electrostatic interaction with SBEβCD. 2D ROESY NMR experiments revealed the insertion of the indole moiety of MTR into the CDs cavity.

NMR spectroscopic studies revealed 1:1 stoichiometry and moderate affinity (logβ_{11}= 3.65) at pD 7.4 for the FDPX·per-6-NH_2βCD complex. However, at pD 2.0, thermodynamically more stable species were inferred: FDPX·per-6-NH_2βCD (log$\beta_{11} \geq$ 4.9) and FDPX·2per-6-NH_2βCD (log$\beta_{12} \geq 8$) was observed. It is rather unique even in the literature, to report such a high affinity system for two oligosaccharides under aqueous conditions. Although no inclusion complex was defined through 2D NMR experiments, we were able to determine the potential interaction site, which involved the IdoA2S moiety and the cationic part of the per-6-NH_2βCD. An in-depth characterization of the acidic degradation of FDPX by NMR suggested desulfation of the pentasaccharide backbone at pD 2.0. By comparing our results with the data found in the literature, it can be concluded that under these conditions the main decomposition product is the result of *N*-desulfation on the trisulfated (GlcNS3S6S) subunit. It has been also proven that under these conditions, the heptacationic cyclodextrin effectively prevents sulfate loss through strong electrostatic interactions.

Our results highlighted the profound impact of the charge state of both host and guest molecules on the complex formation between cyclodextrins and various drugs or bioactive natural products. This influence goes beyond the sole role of stabilizing the complexes; it also has a substantial impact on their stoichiometry and overall structural attributes. Our findings also underscore the importance of carefully considering Job's method, especially when dealing with the formation of complexes that do not adhere to the typical 1:1 stoichiometry.

These revelations have great importance, as they offer assistance not only in the development of various drug formulations but also in the large-scale purification, stabilization and chiral analysis of guest molecules within the analytical community. Furthermore, our findings expand the possibilities for the utilization of CDs, presenting them as promising and innovative solutions to address complex challenges associated with drug formulation, stability, purification and chiral analysis.

SUMMARY

During our experimental work, we aimed at the characterization of the interactions of various cyclodextrins and bioactive molecules focusing on the role of the charge state of both interacting species by NMR spectroscopy. Our work focuses mainly on industrially applied CD-derivatives.

We thoroughly characterized the charge-dependent molecular encapsulation of REM (Veklury®), using various β- and γCD derivatives (βCD, per6-SBEβCD, SBEβCD, γCD, SBEγCD and sugammadex). The stability constants and the structure of the inclusion complexes were investigated by ^{1}H NMR titration and 2D ROESY NMR experiments. Our investigation revealed that introduction of the anionic sulfobutylether-sidechains on the CD hosts contributes to a significant stability enhancement, furthermore the primary side sulfobutylation of the host plays the most critical role in the stability of the inclusion complex. During our work the pK_a value (3.56) of REM was determined experimentally by UV-pH titration for the first time, which contributes to the understanding of the pH-dependent behaviour of the molecule.

In our work, we also investigated the complexation of mitragynine (MTR) - the main alkaloid of the kratom plant - with native βCD and its anionic derivative SBEβCD. ^{1}H NMR titrations revealed weak interaction (logβ_{11} = 0.8; MTR·βCD) between MTR and βCD, whereas a much stronger interaction was determined for SBEβCD (logβ_{11}=3.68, logβ_{21}= 6.87). Our results will be used in the future to investigate different inclusion complexes of structurally related indole and oxindole kratom alkaloids as those are promising skeletons in drug development due to their remarkable opioid-like effects.

In the presented study we characterized intermolecular interactions between the polyanionic, anticoagulant agent FDPX and the polycationic per6-NH_2-βCD. Stoichiometry and complex stability constants were determined at two different pH values by ^{1}H NMR titrations. Based on 2D ROESY and NOESY NMR experiments outer-sphere, electrostatic-driven complex formulation was determined. The degradation of FDPX under acidic conditions were also investigated. Our NMR and MS results prove that the degradation is manifested by loss of a sulfate group, which appears on the trisulfated GlcNS3S6S subunit, in the form of *N*-desulfation.

REFERENCES

1. Crini G. Review: A history of cyclodextrins. Chem Rev. 2014;114(21):10940–75.
2. Szente L, Szemán J. Cyclodextrins in analytical chemistry: Host-guest type molecular recognition. Anal Chem. 2013;85(17):8024–30.
3. Dhiman P, Bhatia M. Pharmaceutical applications of cyclodextrins and their derivatives. J Incl Phenom Macrocycl Chem. 2020;98(3–4):171–86.
4. Szente L, Szejtli J. Highly soluble cyclodextrin derivatives: Chemistry, properties, and trends in development. Adv Drug Deliv Rev. 1999;36(1):17–28.
5. Bricout H, Hapiot F, Ponchel A, Tilloy S, Monflier E. Chemically modified cyclodextrins: An attractive class of supramolecular hosts for the development of aqueous biphasic catalytic processes. Sustainability. 2009;1(4):924–45.
6. Liu L, Guo QX. The driving forces in the inclusion complexation of cyclodextrins. Journal of Inclusion Phenomena. 2002;42(1–2):1–14.
7. Matencio A, Navarro-Orcajada S, García-Carmona F, López-Nicolás JM. Applications of cyclodextrins in food science. A review. Trends Food Sci Technol. 2020;104(July):132–43.
8. Jansook P, Ogawa N, Loftsson T. Cyclodextrins: structure, physicochemical properties and pharmaceutical applications. Int J Pharm [Internet]. 2018;535(1–2):272–84. Available from: https://doi.org/10.1016/j.ijpharm.2017.11.018
9. M Maheriya P. Cyclodextrin: A Promising Candidate in Enhancing Oral Bioavailability of poorly Water Soluble Drugs. MOJ Bioequivalence & Bioavailability. 2017;3(3):60–3.
10. Onn G, Loh K, Tze Y, Tan F, Peh KK. Enhancement of norfloxacin solubility via inclusion complexation with β-cyclodextrin and its derivative hydroxypropyl-β-cyclodextrin. Asian J Pharm Sci [Internet]. 2016 [cited 2023 Nov 12];11:536–46. Available from: http://dx.doi.org/10.1016/j.ajps.2016.02.009
11. Tárkányi G. Quantitative approach for the screening of cyclodextrins by nuclear magnetic resonance spectroscopy in support of chiral separations in liquid chromatography and capillary electrophoresis: Enantioseparation of norgestrel with α-, β- and γ-cyclodextrins. J Chromatogr A. 2002;961(2):257–76.

12. Krois D, Brinker UH. Induced circular dichroism and UV-VIS absorption spectroscopy of cyclodextrin inclusion complexes: Structural elucidation of supramolecular azi-adamantane. J Am Chem Soc [Internet]. 1998 Nov 18 [cited 2023 Nov 12];120(45):11627–32. Available from: https://pubs.acs.org/sharingguidelines
13. Ujj D, Kalydi E, Malanga M, Varga E, Sohajda T, Béni S, Benkovics G. Sugammadex analogue cyclodextrins as chiral selectors for enantioseparation of cathinone derivatives by capillary electrophoresis. J Chromatogr A [Internet]. 2022;1683:463506. Available from: https://doi.org/10.1016/j.chroma.2022.463506
14. Kuhn R, Stoecklin F, Erni F. Chiral separations by host-guest complexation with cyclodextrin and crown ether in capillary zone electrophoresis. Chromatographia. 1992;33(1–2):32–6.
15. Fanali S, Chankvetadze B. Some thoughts about enantioseparations in capillary electrophoresis. Electrophoresis [Internet]. 2019 Sep 1 [cited 2023 Oct 6];40(18–19):2420–37. Available from: https://pubmed.ncbi.nlm.nih.gov/31081552/
16. Ueda H, Ou D, Endo T, Nagase H, Tomono K, Nagai T. Evaluation of a sulfobutyl ether β-cyclodextrin as a solubilizing/stabilizing agent for several drugs. Drug Dev Ind Pharm. 1998;24(9):863–7.
17. Castillo MLR Del, López-Tobar E, Sanchez-Cortes S, Flores G, Blanch GP. Stabilization of curcumin against photodegradation by encapsulation in gamma-cyclodextrin: A study based on chromatographic and spectroscopic (Raman and UV-visible) data. Vib Spectrosc [Internet]. 2015;81:106–11. Available from: http://dx.doi.org/10.1016/j.vibspec.2015.10.008
18. Easton CJ. Cyclodextrin-based catalysts and molecular reactors*. Pure Appl Chem. 2005;77(11):1865–71.
19. Nag K, Singh D, Shetti A, Kumar H, Sivashanmugam T, Parthasarathy S. Sugammadex: A revolutionary drug in neuromuscular pharmacology. Anesth Essays Res. 2013;7(3):302.
20. Schönbeck C. Charge Determines Guest Orientation: A Combined NMR and Molecular Dynamics Study of β-Cyclodextrins and Adamantane Derivatives. Journal of Physical Chemistry B. 2018;122(18):4821–7.

21. Yamamoto Y, Inoue Y. NMR Studies of Cyclodextrin Inclusion Complex. J Carbohydr Chem. 1989;8(1):29–46.
22. Fielding L. Determination of association constants (K(a)) from solution NMR data. Tetrahedron. 2000;56(34):6151–70.
23. Al-Soufi W, Cabrer PR, Jover A, Budal RM, Tato JV. Determination of second-order association constants by global analysis of 1H and 13C NMR chemical shifts. Steroids. 2003;68(1):43–53.
24. Schneider HJ, Hacket F, Rüdiger V, Ikeda H. NMR studies of cyclodextrins and cyclodextrin complexes. Chem Rev. 1998;98(5):1755–85.
25. Zoppi A, Quevedo MA, Longhi MR. Specific binding capacity of β-cyclodextrin with cis and trans enalapril: Physicochemical characterization and structural studies by molecular modeling. Bioorg Med Chem. 2008;16(18):8403–12.
26. Brand T, Cabrita EJ, Berger S. Intermolecular interaction as investigated by NOE and diffusion studies. Prog Nucl Magn Reson Spectrosc. 2005 Sep 1;46(4):159–96.
27. Neuhaus D. Nuclear Overhauser Effect. Encyclopedia of Magnetic Resonance. 2011;1–16.
28. Pessine FBT, Calderini A, Alexandrino GL. Review: Cyclodextrin Inclusion Complexes Probed by NMR Techniques. In: Kim D, editor. Magnetic Resonance Spectroscopy [Internet]. Rijeka: IntechOpen; 2012. p. 237–64. Available from: https://doi.org/10.5772/32029
29. FDA Approves First Treatment for COVID-19 [Internet]. Available from: https://www.fda.gov/news-events/press-announcements/fda-approves-first-treatment-covid-19
30. Wu F, Zhao S, Yu B, Chen YM, Wang W, Song ZG, Hu Y, Tao ZW, Tian JH, Pei YY, Yuan ML, Zhang YL, Dai FH, Liu Y, Wang QM, Zheng JJ, Xu L, Holmes EC, Zhang YZ. A new coronavirus associated with human respiratory disease in China. Nature. 2020;579(7798):265–9.
31. Zhou P, Yang XL, Wang XG, Hu B, Zhang L, Zhang W, Si HR, Zhu Y, Li B, Huang CL, Chen HD, Chen J, Luo Y, Guo H, Jiang RD, Liu MQ, Chen Y, Shen XR, Wang X, Zheng XS, Zhao K, Chen QJ, Deng F, Liu LL, Yan B, Zhan FX, Wang YY, Xiao GF, Shi ZL. A pneumonia outbreak associated with a new

coronavirus of probable bat origin. Nature [Internet]. 2020;579(7798):270–3. Available from: https://doi.org/10.1038/s41586-020-2012-7

32. Warren TK, Jordan R, Lo MK, Ray AS, Mackman RL, Soloveva V, Siegel D, Perron M, Bannister R, Hui HC, Larson N, Strickley R, Wells J, Stuthman KS, Van Tongeren SA, Garza NL, Donnelly G, Shurtleff AC, Retterer CJ, Gharaibeh D, Zamani R, Kenny T, Eaton BP, Grimes E, Welch LS, Gomba L, Wilhelmsen CL, Nichols DK, Nuss JE, Nagle ER, Kugelman JR, Palacios G, Doerffler E, Neville S, Carra E, Clarke MO, Zhang L, Lew W, Ross B, Wang Q, Chun K, Wolfe L, Babusis D, Park Y, Stray KM, Trancheva I, Feng JY, Barauskas O, Xu Y, Wong P, Braun MR, Flint M, Mcmullan LK, Chen SS, Fearns R, Swaminathan S, Mayers DL, Spiropoulou CF, Lee WA, Nichol ST, Cihlar T, Bavari S. Therapeutic efficacy of the small molecule GS-5734 against Ebola virus in rhesus monkeys. Nature. 2016;

33. Humeniuk R, Mathias A, Cao H, Osinusi A, Shen G, Chng E, Ling J, Vu A, German P. Safety, Tolerability, and Pharmacokinetics of Remdesivir, An Antiviral for Treatment of COVID-19, in Healthy Subjects. Vol. 13, Clinical and Translational Science. 2020. 896–906 p.

34. Cao Y chen, Deng Q xin, Dai S xue. Remdesivir for severe acute respiratory syndrome coronavirus 2 causing COVID-19: An evaluation of the evidence. Travel Med Infect Dis [Internet]. 2020;35:101647. Available from: https://doi.org/10.1016/j.tmaid.2020.101647

35. Takayama H. Chemistry and Pharmacology of Analgesic Indole Alkaloids from the Rubiaceous Plant, Mitragyna speciosa. Chem Pharm Bull (Tokyo). 2004 Aug;52(8):916–28.

36. Jansen KLR, Prast CJ. Ethnopharmacology of kratom and the Mitragyna alkaloids. J Ethnopharmacol. 1988;23(1):115–9.

37. Hassan Z, Muzaimi M, Navaratnam V, Yusoff NHM, Suhaimi FW, Vadivelu R, Vicknasingam BK, Amato D, von Hörsten S, Ismail NIW, Jayabalan N, Hazim AI, Mansor SM, Müller CP. From Kratom to mitragynine and its derivatives: Physiological and behavioural effects related to use, abuse, and addiction. Neurosci Biobehav Rev [Internet]. 2013;37(2):138–51. Available from: http://dx.doi.org/10.1016/j.neubiorev.2012.11.012

38. Brown PN, Lund JA, Murch SJ. A botanical, phytochemical and ethnomedicinal review of the genus Mitragyna korth: Implications for products sold as kratom. J Ethnopharmacol [Internet]. 2017;202(March):302–25. Available from: http://dx.doi.org/10.1016/j.jep.2017.03.020
39. Ramachandram DS, Damodaran T, Zainal H, Murugaiyah V, Ramanathan S. Pharmacokinetics and pharmacodynamics of mitragynine, the principle alkaloid of Mitragyna speciosa: Present knowledge and future directions in perspective of pain. J Basic Clin Physiol Pharmacol. 2020;31(1):1–8.
40. Babu KM, McCurdy CR, Boyer EW. Opioid receptors and legal highs: Salvia divinorum and Kratom. Clin Toxicol. 2008;46(2):146–52.
41. Harun N, Kamaruzaman NA, Mohamed Sofian Z, Hassan Z. Mini review: Potential therapeutic values of mitragynine as an opioid substitution therapy. Neurosci Lett. 2022 Mar 16;773:136500.
42. Boyer EW, Babu KM, Adkins JE, McCurdy CR, Halpern JH. Self-treatment of opioid withdrawal using kratom (Mitragynia speciosa korth). Addiction [Internet]. 2008 Jun 1 [cited 2022 Jan 3];103(6):1048–50. Available from: https://onlinelibrary.wiley.com/doi/full/10.1111/j.1360-0443.2008.02209.x
43. Kruegel AC, Gassaway MM, Kapoor A, Váradi A, Majumdar S, Filizola M, Javitch JA, Sames D. Synthetic and Receptor Signaling Explorations of the Mitragyna Alkaloids: Mitragynine as an Atypical Molecular Framework for Opioid Receptor Modulators. J Am Chem Soc [Internet]. 2016 Jun 1 [cited 2023 Nov 12];138(21):6754–64. Available from: https://pubs.acs.org/sharingguidelines
44. Váradi A, Marrone GF, Palmer TC, Narayan A, Szabó MR, Le Rouzic V, Grinnell SG, Subrath JJ, Warner E, Kalra S, Hunkele A, Pagirsky J, Eans SO, Medina JM, Xu J, Pan YX, Borics A, Pasternak GW, McLaughlin JP, Majumdar S. Mitragynine/Corynantheidine Pseudoindoxyls As Opioid Analgesics with Mu Agonism and Delta Antagonism, Which Do Not Recruit β-Arrestin-2. J Med Chem [Internet]. 2016 Sep 22 [cited 2023 Nov 12];59(18):8381–97. Available from: https://pubs.acs.org/sharingguidelines
45. Singh D, Müller CP, Vicknasingam BK. Kratom (Mitragyna speciosa) dependence, withdrawal symptoms and craving in regular users. Drug Alcohol Depend. 2014 Jun 1;139:132–7.

46. Swogger MT, Walsh Z. Kratom use and mental health: A systematic review. Drug Alcohol Depend. 2018 Feb 1;183:134–40.
47. Field E. Mitragynine and Mitraversine. Journal of the Chemical Society Transaction. 1921;119:887–91.
48. Naimy H, Leymarie N, Bowman MJ, Zaia J. Characterization of heparin oligosaccharides binding specifically to antithrombin III using mass spectrometry. Biochemistry. 2008;47(10):3155–61.
49. Mulloy B, Hogwood J, Gray E, Lever R, Page CP. Pharmacology of Heparin and Related Drugs. Pharmacol Rev. 2015;68(1):76–141.
50. Linhardt RJ. 2003 Claude S. Hudson award address in carbohydrate chemistry. Heparin: Structure and activity. J Med Chem. 2003;46(13):2551–64.
51. Jones CJ, Beni S, Limtiaco JFK, Langeslay DJ, Larive CK. Heparin Characterization: Challenges and Solutions. Annual Review of Analytical Chemistry. 2011;4(1):439–65.
52. Gray E, Mulloy B, Barrowcliffe TW. Heparin and low-molecular-weight heparin. Thromb Haemost. 2008;99(5):807–18.
53. Zhang Y, Zhang M, Tan L, Pan N, Zhang L. The clinical use of Fondaparinux: A synthetic heparin pentasaccharide [Internet]. 1st ed. Vol. 163, Progress in Molecular Biology and Translational Science. Elsevier Inc.; 2019. 41–53 p. Available from: http://dx.doi.org/10.1016/bs.pmbts.2019.02.004
54. Donat F, Duret JP, Santoni A, Cariou R, Necciari J, Magnani H, De Greef R. The pharmacokinetics of fondaparinux sodium in healthy volunteers. Clin Pharmacokinet [Internet]. 2002 Nov 28 [cited 2023 Aug 11];41(SUPPL. 2):1–9. Available from: https://link.springer.com/article/10.2165/00003088-200241002-00001
55. Snodgrass MN, Shields J, Rai H. Efficacy and Safety of Fondaparinux in Patients with Suspected Heparin-Induced Thrombocytopenia. Clinical and Applied Thrombosis/Hemostasis [Internet]. 2016 Nov 1 [cited 2023 Aug 11];22(8):712–7. Available from: https://journals.sagepub.com/doi/10.1177/1076029616646873
56. Schroeder M, Hogwood J, Gray E, Mulloy B, Hackett AM, Johansen KB. Protamine neutralisation of low molecular weight heparins and their oligosaccharide components. Anal Bioanal Chem. 2011;399(2):763–71.

57. Crowther MA, Berry LR, Monagle PT, Chan AKC. Mechanisms responsible for the failure of protamine to inactivate low-molecular-weight heparin. Br J Haematol. 2002;116(1):178–86.
58. Kalaska B, Kaminski K, Sokolowska E, Czaplicki D, Kujdowicz M, Stalinska K, Bereta J, Szczubialka K, Pawlak D, Nowakowska M, Mogielnicki A. Nonclinical evaluation of novel cationically modified polysaccharide antidotes for unfractionated heparin. PLoS One. 2015;10(3):1–21.
59. Malanga M, Fejős I, Varga E, Benkovics G, Darcsi A, Szemán J, Béni S. Synthesis, analytical characterization and capillary electrophoretic use of the single-isomer heptakis-(6-O-sulfobutyl)-beta-cyclodextrin. J Chromatogr A. 2017 Sep 8;1514:127–33.
60. Job P. Formation and stability of inorganic complexes in solution. Ann Chim (Paris). 1928;9:113–203.
61. Solution Equilibria Analysis with the OPIUM Computer Program [Internet]. [cited 2023 Nov 11]. Available from: http://web.natur.cuni.cz/~kyvala/opium.html
62. Alderighi L, Gans P, Ienco A, Peters D, Sabatini A, Vacca A. Hyperquad simulation and speciation (HySS): a utility program for the investigation of equilibria involving soluble and partially soluble species. Coord Chem Rev [Internet]. 1999 [cited 2023 Nov 12];184:311–8. Available from: http://www.eawag.ch/soft/
63. ORCHESTRA | Geochemical and Transport Modelling [Internet]. [cited 2023 Nov 11]. Available from: http://orchestra.meeussen.nl/
64. Szakács Z, Noszál B. Determination of dissociation constants of folic acid, methotrexate, and other photolabile pteridines by pressure-assisted capillary electrophoresis. Electrophoresis. 2006;27(17):3399–409.
65. Artese A, Svicher V, Costa G, Salpini R, Di Maio VC, Alkhatib M, Ambrosio FA, Santoro MM, Assaraf YG, Alcaro S, Ceccherini-Silberstein F. Current status of antivirals and druggable targets of SARS CoV-2 and other human pathogenic coronaviruses. Drug Resistance Updates. 2020 Dec 1;53:100721.
66. Szente L, Puskás I, Sohajda T, Varga E, Vass P, Nagy ZK, Farkas A, Várnai B, Béni S, Hazai E. Sulfobutylether-beta-cyclodextrin-enabled antiviral remdesivir:

Characterization of electrospun- and lyophilized formulations. Carbohydr Polym. 2021;264(April).

67. Kalydi E, Malanga M, Ujj D, Benkovics G, Szakács Z, Béni S. Fully Symmetric Cyclodextrin Polycarboxylates: How to Determine Reliable Protonation Constants from NMR Titration Data. Int J Mol Sci. 2022;23(22).
68. Szente L, Fenyvesi É. Cyclodextrin-Lipid Complexes: Cavity Size Matters. Struct Chem. 2017;28(2):479–92.
69. Béni S, Sohajda T, Neumajer G, Iványi R, Szente L, Noszál B. Separation and characterization of modified pregabalins in terms of cyclodextrin complexation, using capillary electrophoresis and nuclear magnetic resonance. J Pharm Biomed Anal. 2010;51:842–52.
70. Várnai B, Zsila F, Szakács Z, Garádi Z, Malanga M, Béni S. Sulfobutylation of Beta-Cyclodextrin Enhances the Complex Formation with Mitragynine: An NMR and Chiroptical Study. Int J Mol Sci. 2022;23(7).
71. Dignam CF, Randall LA, Blacken RD, Cunningham PR, Lester SKG, Brown MJ, French SC, Aniagyei SE, Wenzel TJ. Carboxymethylated cyclodextrin derivatives as chiral NMR discriminating agents. Tetrahedron Asymmetry. 2006 Apr 18;17(8):1199–208.
72. Carvalho LB de, Burusco KK, Jaime C, Venâncio T, Carvalho AFS de, Murgas LDS, Pinto L de MA. Complexes between methyltestosterone and β-cyclodextrin for application in aquaculture production. Carbohydr Polym [Internet]. 2018;179:386–93. Available from: http://dx.doi.org/10.1016/j.carbpol.2017.09.023
73. Ramanathan S, Parthasarathy S, Murugaiyah V, Magosso E, Tan SC, Mansor SM. Understanding the physicochemical properties of mitragynine, a principal alkaloid of Mitragyna speciosa, for preclinical evaluation. Molecules. 2015 Mar 1;20(3):4915–27.
74. Wenz G, Strassnig C, Thiele C, Engelke A, Morgenstern B, Hegetschweiler K. Recognition of ionic guests by ionic β-cyclodextrin derivatives. Chemistry - A European Journal. 2008;14(24):7202–11.

75. Wang HM, Loganathan D, Linhardt RJ. Determination of the pK(a) of glucuronic acid and the carboxy groups of heparin by 13C-nuclear-magnetic-resonance spectroscopy. Biochemical Journal. 1991;278(3):689–95.
76. Ulatowski F, Dabrowa K, Bałakier T, Jurczak J. Recognizing the Limited Applicability of Job Plots in Studying Host-Guest Interactions in Supramolecular Chemistry. Journal of Organic Chemistry. 2016;81(5):1746–56.
77. Brynn Hibbert D, Thordarson P. The death of the Job plot, transparency, open science and online tools, uncertainty estimation methods and other developments in supramolecular chemistry data analysis. Chemical Communications. 2016;52(87):12792–805.
78. Kalsson A, Singh SK. Acid hydrolysis of sulphated polysaccharides. Desulphation and the effect on molecular mass. Carbohydr Polym. 1999;38(1):7–15.
79. Seto SP, Miller T, Temenoff JS. Effect of selective heparin desulfation on preservation of bone morphogenetic protein-2 bioactivity after thermal stress. Bioconjug Chem. 2015;26(2):286–93.
80. Kozlowski AM, Yates EA, Roubroeks JP, Tømmeraas K, Smith AM, Morris GA. Hydrolytic Degradation of Heparin in Acidic Environments: Nuclear Magnetic Resonance Reveals Details of Selective Desulfation. ACS Appl Mater Interfaces. 2021;13(4):5551–63.
81. Kozlowski AM, Dinu V, MacCalman T, Smith AM, Roubroeks JP, Yates EA, Harding SE, Morris GA. Heparin in Acid and Alkaline Environments—A Study of the Correlations between Hydrodynamic Properties and Desulphation. Polysaccharides. 2023;4(2):88–98.
82. Várnai B, Grabarics M, Szakács Z, Pagel K, Malanga M, Sohajda T, Béni S. Structural characterization of fondaparinux interaction with per-6-amino-beta-cyclodextrin: An NMR and MS study. J Pharm Biomed Anal. 2021;197.

BIBLIOGRAPHY OF THE CANDIDATE'S PUBLICATIONS

Regarding the topic of the thesis:

Várnai B, Grabarics M, Szakács Z, Pagel K, Malanga M, Sohajda T, Béni S. Structural characterization of fondaparinux interaction with per-6-amino-beta-cyclodextrin: An NMR and MS study. J Pharm Biomed Anal. 2021;197.

Várnai B, Malanga M, Sohajda T, Béni S. Molecular interactions in remdesivir-cyclodextrin systems. J Pharm Biomed Anal 2022;209:114482;

Várnai B, Zsila F, Szakács Z, Garádi Z, Malanga M, Béni S. Sulfobutylation of Beta-Cyclodextrin Enhances the Complex Formation with Mitragynine: An NMR and Chiroptical Study. Int J Mol Sci. 2022;23(7).

Other publications:

Varga E, Benkovics G, Darcsi A, **Várnai B**, Sohajda T, Malanga M, Béni S. Comparative analysis of the full set of methylated β-cyclodextrins as chiral selectors in capillary electrophoresis. Electrophoresis. 2019;40(21):2789–98.

Szente L, Puskás I, Sohajda T, Varga E, Vass P, Nagy ZK, Farkas A, **Várnai B**, Béni S., Hazai E. Sulfobutylether-beta-cyclodextrin-enabled antiviral remdesivir: Characterization of electrospun- and lyophilized formulations. Carbohydr Polym. 2021 Jul 15;264:118011.

Fejős I, Tóth G, **Várnai B**, Szabó ZI, Köteles I, Malanga M, Béni S. Enantioseparation of solriamfetol and its major impurity phenylalaninol by capillary electrophoresis using sulfated gamma cyclodextrin. Electrophoresis. 2021 Sep 1;42(17–18):1818–25.

Valiyeva A, Felegyi-Tóth CA, **Várnai B**, Garaev E, Béni S, Kursinszki L. Characterization of alkaloid profile of Hyoscyamus reticulatus L. and Atropa belladonna subsp. caucasica (Kreyer) Avet by LC-MS and NMR. Nat Prod Res. 2023; 37(19):3357–62.

ACKNOWLEDGEMENTS

Although only one author's name appears on the first page of this work, this doctoral thesis was made possible by the collective contribution of many helping hands.

Firstly, I would like to express my gratitude to my supervisor, Dr. Szabolcs Béni, whose unwavering guidance and steadfast support guided my doctoral work throughout. I would also like to thank him for the time and effort he has devoted to my professional development.

Furthermore, I would like to thank Dr. Zoltán Szakács (Richter Gedeon Nyrt.) for his tireless assistance in the study of the equilibrium chemistry of cyclodextrin complexes.

I am indebted to Dr. Milo Malanga for the cyclodextrins needed for our experiments, as well as to Cyclolab Kft. and CarboHyde Zrt.

I am genuinely grateful for the support of my colleagues at the Department of Pharmacognosy, Semmelweis University, who have contributed greatly to my studies and research. Their company encouraged me and created a positive environment that I looked forward to being part of every day. Special thanks to Eszter Kalydi, Zsófia Garádi and Csenge Anna Felegyi-Tóth for their support and for helping me through the hard and challenging times.

Last but certainly not least, my deepest thanks go to my family and friends for their unwavering support, understanding, and encouragement throughout this challenging journey.